NTNU – Trondheim
Norwegian University of
Science and Technology

Thermoelectric Properties of A-site Deficient Lanthanum Substituted Strontium Titanate

Thomas Emdal Loland

Materials Science and Engineering
Submission date: June 2014
Supervisor: Kjell Wiik, IMTE

Norwegian University of Science and Technology
Department of Materials Science and Engineering

Declaration

I hereby declare that the work presented in this document has been performed independently and in accordance with the rules and regulations of the Norwegian University of Science and Technology (NTNU), except from the production of the samples and some results that were collected by people that have been credited in the preface.

Trondheim, 23 June 2014

Thomas Emdal Loland

Preface

The work in this thesis has been performed at the Department of Materials Science and Engineering on the Norwegian University of Science and Technology (NTNU) during the spring part of 2014.

Several people have been very helpful in the experimental part of this thesis, and deserves my gratitude. Ahead of all others, my supervisor Professor Kjell Wiik, thank you for guiding me through this thesis. Your patience and good advice have been very helpful. For the production of the samples investigated in this thesis, I would like to thank Professor Mari-Ann Einarsrud (NTNU) and Professor Mats Johnsson (Stockholm University). The difficult cutting of the samples into shape was performed by staff engineer Astrid Salvesen (NTNU). The two TEM-sessions that were performed at NTNU were operated by Research Scientist Per Erik Wullum (SINTEF), along with the polymorph identification from the diffraction patterns recorded. I would also like to thank NorTEM for the financial support in running the TEM-samples at NTNU. For the TEM-session that was performed at Stockholm University, I would like to thank operator PhD Tom Willhammar from Stockholm University. For your help with the Laser Flash apparatus, I would like to thank Anne Støre (SINTEF) and Post doc Sophie Beatrice Weber (NTNU). For help in understanding the Probostat oven used for Seebeck coefficient measurements, I would like to thank Belma Talic. For your help in understanding the operation of the 4-point electrical conductivity oven, thank you to Sandra Helen Skjærvø and Espen Tjønneland Wefring. Eli-Beate Larsen performed the dilatometry measurements. Also the technical, staff in general, at the Department of Materials Science and Engineering at the Norwegian University of Science and Technology deserves some attention, you have been very helpful with knowledge and experimental aid.

Thank you all for your help.

I would also like to thank my family for their support and enthusiasm during my degree.

Abstract

The n-type thermoelectric material $(La_{0.12}Sr_{0.88})_{0.95}TiO_{3-\partial}$ was sintered with the spark plasma sintering method at different temperatures and pressures. This was done to reduce the thermal conductivity of the material and increase its thermoelectric figure of merit. The samples sintered at the lowest temperatures had less grain growth, and hence a lower thermal conductivity. The thermal conductivity of these samples were significantly lower than measurements reported by Sele[1] on the same stoichiometry. The thermal conductivity reduction in the samples are mostly attributed to small grain size reducing the phonon mean free path, and hence lattice conduction in the samples. Some phase segregation was observed in the samples sintered at highest temperature. The secondary phase did not display any significant impact on the thermal conductivity of the samples. The thermal transport by electrons is close to zero in most of the samples because of a low charge carrier concentration. Since the carrier concentration inflict all the important parameters of a thermoelectric material, an optimum concentration exist. This concentration is well above what was observed in this work. The electrical conductivity and the Seebeck coefficient are both heavily reliant on the charge carrier concentration in the material. For this reason, some strategies for increasing the amount of charge carriers in future experiments have been presented. The presented work has further advanced the understanding of the investigated material. This is an important step toward being able to manufacture a n-type thermoelectric material, that is oxide-based and market viable.

Sammendrag

Det termoelektriske n-type materialet $(La_{0.12}Sr_{0.88})_{0.95}TiO_{3-\partial}$ ble sintret ved hjelp av gnist-plasma sintringsmetoden ved forskjellige temperaturer og trykk. Dette ble gjort for å redusere varmeledningsevnen til materialet slik at den termoelektriske yteevnen til materialet økes. Prøvene som ble sintret ved lavest temperatur hadde lavere varmeledningsevne som følge av mindre kornvekst. Varmeledningsevnen til prøvene var betydelig lavere enn de rapportert av Sele[1] på samme støkiometri. Liten kornstørrelse blir gitt mesteparten av æren for den reduserte varmeledningsevnen som følge av en reduksjon i midlere fri veilengde for gitterkonduktivitet i materialet. Noe fasesegregering ble funnet i prøvene som ble sintret ved høyest temperatur. Sekundærfasen så ikke ut til å ha noen betydelig effekt på varmeledningsevnen til prøvene. Varmeledning av elektroner er neglisjerbar i de fleste prøvene på grunn av et lavt innhold av ladningsbærere. Den lave ladningsbærerkonsentrasjonen har innvirkning på alle egenskapene som er av betydning for termoelektrisitet. En ladningsbærerkonsentrasjon finnes derfor i denne modellen, som gir det beste forholdet mellom disse ved en definert ladningsbærerkonsentrasjon. Denne konsentrasjonen vil resultere i den beste termoelektriske yteevnen for materialet. Denne konsentrasjonen er betydelig over den som er observert i dette arbeidet. Både den elektriske ledningsevnen og Seebeck koeffisienten til materialet er veldig avhengig av ladningsbærerkonsentrasjon. Siden denne er lav, har noen mulige strategier for økning av denne i fremtidig arbeid, blitt presentert. Det presenterte arbeidet har økt forståelsen for materialet og er et viktig steg mot produksjon av et markedsdyktig n-type oksidbasert termoelektrisk materiale.

Contents

1 Introduction

1.1 Background

One of the great challenges of current generations in the world is the climate changes. The greenhouse gases that are emitted by many of our industrial processes are drastically changing the environment for the worse. Measures need to be taken in order to cope with these problems. Many politicians are talking a lot about capturing the climate gases and storing them. Even if such technologies may be an important step in the right direction, it is not the only one possible. By increasing the overall efficiency of the industrial processes, less energy will be needed and fewer electrical plants are thereby needed. This can decrease the need for burning fossil fuels in order to produce electricity. There are several ways to increase the efficiency of an industrial process, one being harvesting waste heat. Instead of letting waste heat from energy demanding industrial processes go to waste, it could be captured and converted into useful energy. At present day, many companies use turbine based heat collection systems, or just sending warm cooling water to locations where heating is required. There are however also other possibilities. One of these being the use of thermoelectric materials. These are solid-state devices, which means they have no moving parts. By having a solid-state device instead of i.e. a turbine, you neglect many potential disasters, but also the need for maintenance and repair will be reduced. Downtime on this type of industrial processes are often costly and hence a system that requires little looking after would be attractive. The thermoelectric materials that dominate the market at present are often made from heavy elements that are viewed as toxic to the environment. One way to circumvent this problem is to use oxide-based materials, as almost all conducting material display thermoelectric phenomena[2]. The properties determining the efficiency of the oxides are however still not where they should be to become commercially viable. The efficiency of other thermoelectric material are still too far ahead. In particular, the n-doped materials that are required for thermoelectric devices have proven a bit tricky to fabricate. There is however great promise in some candidate materials. One of these materials is the Lanthanum-doped $SrTiO_3$-perovskite, which is the focus material for this work. It is believed that this material have the potential to one day display the properties that makes the material viable on the commercial market. However, some work remain, and this is the task addressed in this thesis.

1.2 Objectives

The material have previously displayed a decent electrical conductivity and Seebeck coefficient. The thermal conductivity of the material do however have a high value. For the intended use of the material, a low thermal conductivity is favorable. The main goal of this thesis is therefore to achieve a low thermal conductivity, while also looking at how the modifications affect the other material properties that are important for thermoelectric applications.

2 Theory

2.1 Thermoelectric concepts

Three processes are important in order to classify a thermoelectric device. These are the Seebeck, Peltier and Thomson effects. Even though these are separate effects, they are intimately connected.

2.1.1 Seebeck effect

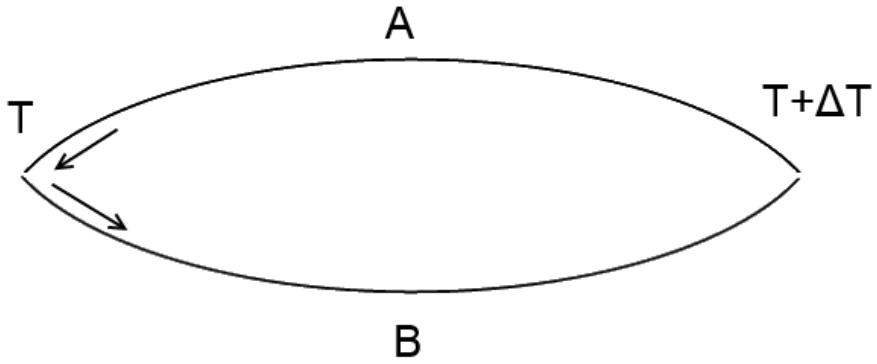

Figure 2.1: The Seebeck effect schematically explained. Material A and material B is on opposite sides, while the junctions between them are held at different temperatures, an electric current will flow.[3]

In the 1820s, Thomas Johann Seebeck discovered the thermoelectric effect by observing that two dissimilar materials that are electrically conductive will cause a flow of electrical current when the junctions between the two are held at different temperatures [3]. The electric current arises from a potential difference that arises in the system. This potential difference changes with temperature and hence the Seebeck coefficient is defined.

$$S = \frac{dV}{dT} \tag{2.1}$$

Where S is the Seebeck coefficient, dV is the potential difference and dT is the temperature difference between the two junctions. For experimental simplicity, the formula can be simplified to

$$S = \frac{\Delta V}{\Delta T} \tag{2.2}$$

The Seebeck coefficient defines the magnitude of the potential difference that arise with a certain temperature difference. This is different for each material, and may be understood by investigating the Fermi-Dirac distributions for the different temperatures in each material [3, 4]. For the n-type material investigated in this thesis, an electron surplus will be produced at the hot side. This surplus is attempted equilibrated by diffusion, and a diffusion current arises. It is important to emphasize that the Seebeck effect and the Volta effect, or contact potential, are two unrelated effects[3].

2.1.2 Peltier effect

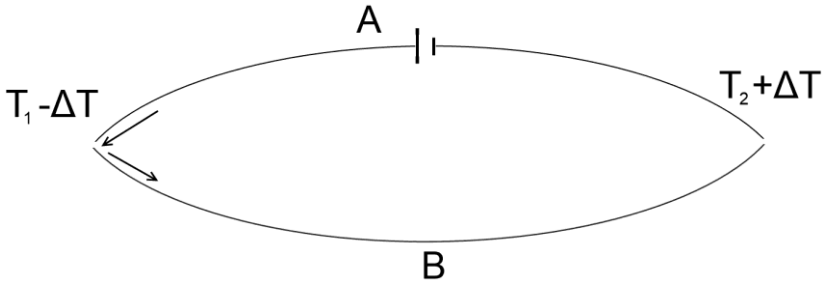

Figure 2.2: Schematic representation of the Peltier effect. A direct current is applied in material A, which causes a temperature difference to arise at the junctions.

When an electrical current is supplied, instead of being harvested, a temperature difference is induced at the material junctions. This is called the Peltier effect and was discovered by Jean Charles Anathase Peltier, which was able to freeze a droplet of water as the first demonstration of the phenomena [3]. The definition of the Peltier coefficient is the reversible change in heat content when one coulomb crosses the junction, with the sign determined by the direction of the current [3, 5]. The absorption or liberation of heat at the junctions is defined as[1]

$$Q_P = (\Pi_A - \Pi_B) \cdot \mathrm{I} = \Pi_{AB} \cdot I = S_{AB} \cdot T \cdot I \qquad (2.3)$$

The transferred heat is Q_P , Π is the Peltier coefficients for the two materials and I is the electrical current running in the material. The equation shows that the signs of the Peltier coefficients and the electrical current determines if the junction will liberate or absorb heat.

2.1.3 Thomson effect

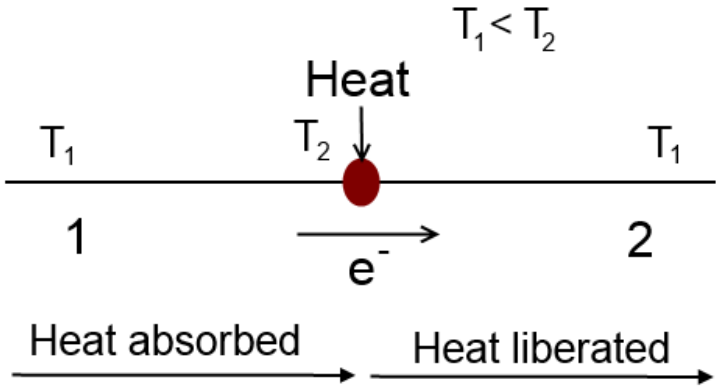

Figure 2.3: Schematic representation of the Thomson effect, which is the transfer of heat by electron movements in a temperature gradient.

The Thomson effect was discovered by William Thomson in 1856 and laid the foundation of the establishment of the field of non-equilibrium thermodynamics by Lars Onsager in 1931[5]. As can be seen from Figure 2.3, the Thomson effect is basically the transport of heat energy by a moving electron. An electron moving

against a positive thermal gradient(becoming hotter), will absorb energy from its surroundings, while an electron moving against a negative thermal gradient will liberate energy to its surroundings[3]. Even if this effect usually is small, it should not be neglected in precision calculations. The amount of absorbed or liberated heat is found by[1]

$$Q_T = \mu \cdot i \cdot \frac{dT}{dx} \tag{2.4}$$

Where Q_T is the transferred heat by the Thomson effect, μ is the Thomson coefficient, i is the current density and dT/dx is the thermal gradient. The Thomson coefficient is connected to the Seebeck coefficient and the Peltier coefficient by the Kelvin relationships [1, 2].

$$\mu = T\frac{dS}{dT} \tag{2.5}$$

$$\Pi = S \cdot T \tag{2.6}$$

2.1.4 Thermoelectric interdependence

As mentioned, these phenomena are quite connected. An equation that resembles that of a reversible heat engine emerges when these three phenomena are linked[3]:

$$S_{AB} \cdot \Delta T = \Pi_{AB}(T + \Delta T) - \Pi_{AB}(T) + (\mu_B - \mu_A) \cdot \Delta T \tag{2.7}$$

Where $S_{AB} \cdot \Delta T$ is the potential generated by the Seebeck effect, $\Pi_{AB}(T + \Delta T)$ is the potential from absorbed heat at the hotter junction (Peltier effect) and $\Pi_{AB}(T)$ is the potential from liberated heat at the colder junction (Peltier effect). $\mu_B \Delta T$ and $\mu_A \Delta T$ respectively, are the potential from the absorption of heat in conductor B and from the liberation of heat in conductor A by the Thomson effect. The temperature dependent generation of potentials is expressed as[3]

$$S_{AB} = \frac{d\Pi_{AB}}{dT} + (\mu_B - \mu_A) \tag{2.8}$$

Where the units of the Seebeck and Thomson effect is V/K and the Peltier coefficient has the unit V. To get the answer in watts, the equation (2.7) should be multiplied by the electric current I.

2.1.5 Figure of merit

The efficiency of a thermoelectric material is defined by[2, 6-8]

$$\eta = \left(\frac{T_{hot} - T_{cold}}{T_{hot}} \right) \left[\frac{\sqrt{1+ZT} - 1}{\sqrt{1+ZT} + \left(T_{cold} / T_{hot} \right)} \right] \tag{2.9}$$

Where η is the efficiency, T_{hot} and T_{cold} is the temperature on the hot and cold side respectively and ZT is the figure of merit for the material. The figure of merit is a dimensionless measure of the ability a material have to efficiently produce thermoelectric power, and is often used to compare the efficiency of thermoelectric materials against each other. The figure of merit is defined as[7-9]

$$ZT = \frac{S^2 T \sigma}{\kappa} \tag{2.10}$$

Here S is the Seebeck coefficient, T is the mean temperature of the material, σ is the electrical conductivity and κ is the thermal conductivity of the material. Even if Z is the 'true', temperature independent, figure of merit, a temperature dependence is often added, since the components determining the value are also temperature dependent. The addition of temperature also makes the value dimensionless.

2.1.6 Seebeck coefficient

The Seebeck coefficient is important in the figure of merit and is approximated by[10]

$$S = \frac{8\pi^2 k_B^2}{3eh^2} m^* T \left(\frac{\pi}{3n} \right)^{\frac{2}{3}} \tag{2.11}$$

Where k_B is Boltzmann's constant, e is the electron charge, h is Planck's constant, m^* is the effective charge carrier mass, T is the absolute temperature and n is the charge carrier concentration, which will be discussed in section 2.2.

2.1.7 Experimental assessment of the Seebeck coefficient

When measuring the Seebeck coefficient of the sample at different temperatures, one need two thermocouples and two electrodes. This is to record both the temperature difference and potential difference between the two sides of the sample. For the thermocouples, S-elements are typically used. The materials used in this element are wires made from pure Pt and an alloy of 90wt% Pt / 10wt% Rh. If the stoichiometry of these wires are somewhat different from this, the Seebeck coefficient for the materials may change slightly. If this happens, the voltage that is recorded at the thermoelectric junction, which is coupled to a temperature, will be slightly different from one where the stoichiometry is correct. It is therefore expected some small differences between thermocouples. In order to compensate

for this, a calibration against each other would be favorable, to determine any differences. This can be done by placing the thermocouples very close to each other inside the oven to have them at a location of small temperature difference. By knowing that the thermocouples are supposed to have quite similar voltage readings, it is possible to estimate the error at different temperatures.

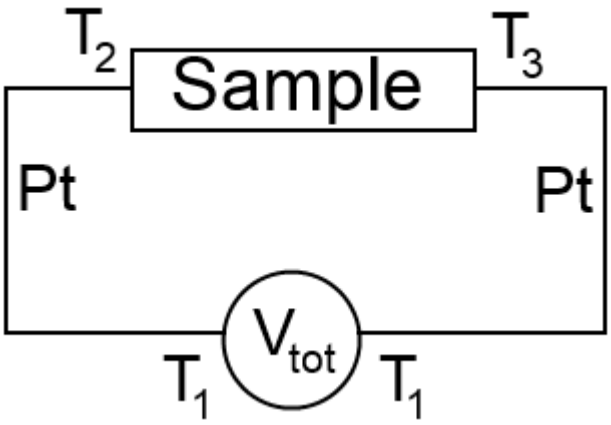

Figure 2.4: A schematic representation of the measurement of the Seebeck coefficient. The voltage contributions from the Pt-wires have to be subtracted to determine the correct Seebeck coefficient for the sample.

The electrode wires are usually Pt. The Seebeck coefficient for this material is well defined at different temperatures[11], and can be found in the appendix. The Seebeck coefficient for Pt is needed in order to be able to compensate for the inherent potential difference in the electrode leads. The electrodes also exhibit thermoelectric properties, and a potential difference will arise because of the temperature difference between electrode locations. From Figure 2.4, the total voltage recorded is a combination of all the contributions

$$V_{tot} = \int_{T_1}^{T_2} S_{Pt} dT + \int_{T_2}^{T_3} S_{Sample} dT + \int_{T_3}^{T_1} S_{Pt} dT \qquad (2.12)$$

From the total voltage, the Seebeck coefficient for the sample is found by subtracting the contributions from the Pt-wires. Since the measurement of a Seebeck coefficient relies on an accurate measurement of both the potential difference and the temperature difference of the sample, these error calculations have some significance to ensure accurate answers.

2.2 Crystal structure and defect chemistry

The stacking of the elements in the material have a significant impact on its properties. It is therefore important to understand what happens to the material on a microscopic level in order to understand its macroscopic properties.

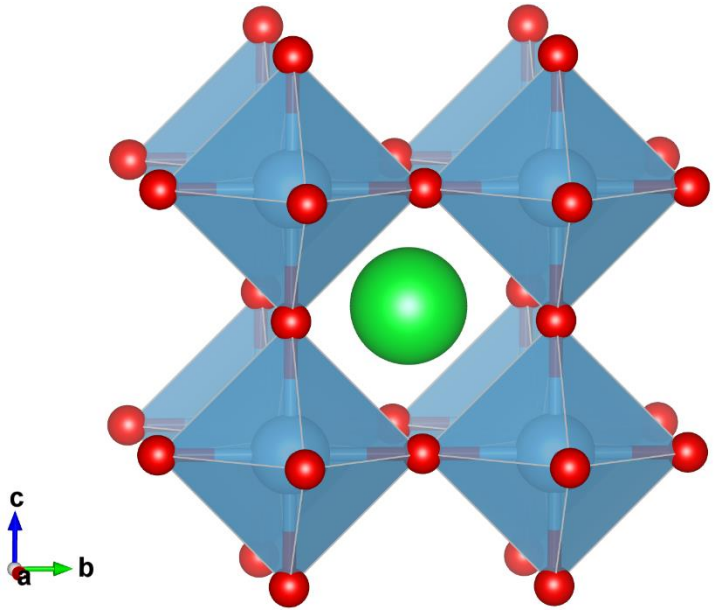

Figure 2.5: $SrTiO_3$ as modeled in VESTA[12] The green atom in the A-site is Sr, the blue atoms in the middle of the octahedral, in the B-site, is Ti, while the red atoms in octahedral positions are oxygen.

2.2.1 Crystal structure

The structure of a material is often closely intertwined with the properties of a material. Strontium Titanate (STO) has the perovskite crystal structure. This structure is based around a cubic lattice structure and therefore have the same lattice parameter, a, on all axes. Perovskites are generally described by the simple formula ABO_3, where A and B refers to different locations in the structure, as shown in Figure 2.5. How the defect chemistry of the material will be affected by changes is largely dependent on the oxidation states of the different elements in the material. The polymorph of the material can also be estimated by looking at the ionic radii of the elements in the material and relating this to Goldschmidt's tolerance factor.

Table 2.1: The possible oxidation states of the atoms used and their ionic radii[13]. The bold oxidation state number represent the most stable state.

Atom	Oxidation state	Ionic radius (pm)
La	**+3**	116
Sr	**+2**	126
Ti	**+4** / +3	60.5 / 67
O	**-2**	140

2.2.2 Goldschmidt's tolerance factor

To maintain a cubic structure, the ionic radii of the elements become important. If the geometrical relations go too far off from the ideal, a distortion of the crystal will occur. The stability of a perovskite phase can be related to its Goldschmidt tolerance factor. This is a simple geometric analysis to investigate if the material will maintain a cubic phase or change into another polymorph when doping a material. This model is however not valid when considering vacancies, because the structure can no longer be considered close packed[14]. For this reason, it is difficult to determine the actual value for the stoichiometry investigated in this work. By using a qualitative approach, it is however possible to somewhat determine the polymorph stability. The tolerance factor is defined as[14, 15]

$$t = \frac{r_A + r_O}{\sqrt{2}\left(r_B + r_O\right)} \tag{2.13}$$

Where t is the tolerance factor, r_A is the ionic radius of the A-site element in the perovskite crystal structure, r_O is the ionic radius of the Oxygen position and r_B is the ionic radius of the B-site element.

Table 2.2: The different polymorphs of ABO_3 associated with their respective intervals in tolerance factor[1].

Structure	Tolerance factor
Hexagonal stacking	t > 1.10
Ideal cubic perovskite	0.89 < t < 1
Orthorombic distortion	0.8 < t < 0.89
Ilmenite	t < 0.8

The tolerance factor, if all Sr^{2+} is substituted with La^{3+}, and Ti^{4+} goes to Ti^{3+}, will be 0.874. For the original phase $SrTiO_3$, the tolerance factor is 0.938. Since the doping with La^{3+} is with only 12% for the material without vacancies, the tolerance factor will drop some, but not as much as down to 0.874. If the change is linear with composition, a value of 0.930 would be reached by this doping. This value is still quite a bit over the lower stability limit for a cubic phase, found in Table 2.2, which lie at 0.89. An Orthorhombic distortion is therefore avoided thus far. To have a complete picture of the stability of the polymorph, the A-site deficiency and level of reduction need to be included in this analysis. As mentioned above, however, vacancies do not combine well with the tolerance factor and a more defined tolerance factor is difficult to acquire.

2.2.3 Lanthanum doping

The doping of STO with La will introduce a surplus electron to the material, with respect to the original Sr. This electron needs to be charge compensated. Since Ti in the structure have an oxidation level of +4, but is also able to have the oxidation state +3, it will compensate the doping by changing oxidation state from +4 to +3, and can be represented by the following Kröger-Vink equation[16]

$$La_2O_3 + 2Ti_{Ti}^{X} \xrightarrow{SrTiO_3} 2La_{Sr}^{\bullet} + 2O_O^X + \frac{1}{2}O_2(g) + 2Ti_{Ti}' \quad (2.14)$$

Since Ti now has the oxidation state of +3 it can be utilized as an electronic conduction center in its location by temporarily going back to +4[16, 17], as will be discussed further under section 2.3.

2.2.4 A-site deficiency

Having an A-site deficiency effectively mean having Strontium vacancies in the material. The results of Neagu and Irvine[18] seem to indicate an association of Strontium and oxygen vacancies in pairs $\left(V_{Sr}''V_O^{\bullet\bullet}\right)$. Similar associations are often called Schottky defects. According to Neagu and Irvine this has also been suggested by theoretical calculations for other perovskite systems. The A-site deficiency introduces positive charges that needs to be charge compensated. As stated above, an oxygen vacancy can do this. The following equation describe this association

$$0(nil) \xrightarrow{SrTiO_3} V_{Sr}'' + V_O^{\bullet\bullet} \quad (2.15)$$

By having an A-site deficiency in the material it is also possible to get exsolutions of TiO_2 in the La-doped STO material[18, 19]. The solubility of excess TiO_2 in $SrTiO_3$ has been reported to be below 0.2mol%[20]. By decreasing the A-site and having a reduced oxygen content, a surplus of Ti in the stoichiometry is no longer energetically favorable, thereby forming TiO_2.

2.2.5 Oxygen reduction and exsolution

Extra Oxygen vacancies will also be charge compensated by the Ti-atoms [17, 18]

$$2Ti_{Ti}^{X} + O_O^X \rightarrow 2Ti_{Ti}' + V_O^{\bullet\bullet} + \frac{1}{2}O_2(g) \quad (2.16)$$

The trivalent Ti-atom electron carrier will be discussed in section 2.3.3. Oxygen diffusion in the lattice have some significance in order to assure a homogeneous reduction of volumes deep inside the sample. The reduction of the sample only

happens on the surface, and hence for the material deeper in the sample, oxygen will have to diffuse toward the surface. In order to be able to have any significant amount of oxygen transport, empty sites are needed. A high occurrence of oxygen vacancies will ensure oxygen ion transport in the lattice. The speed will therefore increase with reduction level. The most important step in this transport is thought to be when the hopping through the triangle defined by Sr-Ti-Sr, which is shown in Figure 2.6[17].

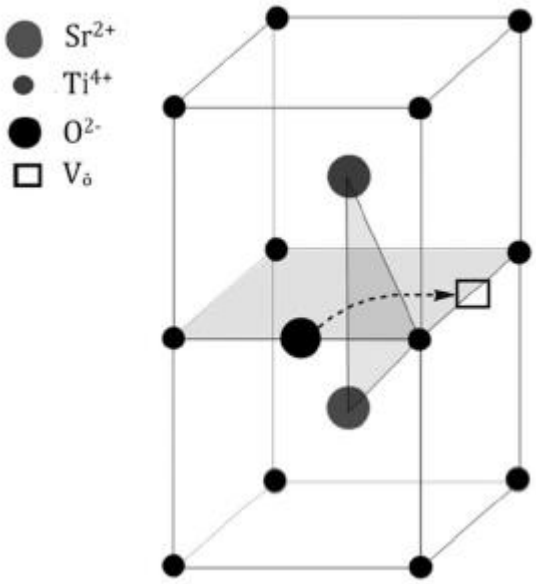

Figure 2.6: A schematic representation of oxygen diffusion in the unit cell[17]. The oxygen have to pass through the area between two Sr-ions and a Ti-ion in order to reach another oxygen position. Most of the oxygen in the unit cell is omitted for clarity.

As mentioned in the section 2.2.4, the reduction of an A-site deficient material has the potential to create exsolutions of TiO_2 in the material. Neagu and Irvine[18] suggested that after reaching an oxygen deficiency limit TiO_2 will separate from the primary phase according to the following equation

$$A_{1-x}TiO_3 \xrightarrow{\text{Reduction}} A_{1-x}TiO_{3-\delta_{\lim}} \xrightarrow{\text{Further reduction}} A_{1-x}Ti_{1-y}O_{3-\delta_{\lim}-yn} + yTiO_n \qquad (2.17)$$

As can be seen from the equation above, this exsolution of TiO_2 will leave the primary phase less A-site deficient. This will change its material properties. The reason for the exsolution of TiO_2 is hence that the solubility limit is reached when reducing the sample beyond a limit[18, 19].

2.2.6 Charge carriers

The amount of charge carriers have a significant impact on both the Seebeck coefficient and the electrical conductivity of the material, as will be shown in later sections. In a simplified view of the defect chemistry of the material, where one expect a conduction band, the equations below explain changing amounts of charge carriers.

$$\begin{aligned}
&\text{La-doping: } La_2O_3 \xrightarrow{SrTiO_3} 2La_{Sr}^{\bullet} + 2O_O^X + \frac{1}{2}O_2(g) + 2\mathrm{e}^- \\
&\text{Oxygen reduction: } 0(\text{nil}) \xrightarrow{SrTiO_3} V_O^{\bullet\bullet} + \frac{1}{2}O_2(g) + 2\mathrm{e}^- \\
&\text{A-site vacancies: } 0(\text{nil}) \xrightarrow{SrTiO_3} V_{Sr}'' + V_O^{\bullet\bullet}
\end{aligned} \tag{2.18}$$

The charge carriers are considered to be localized at the reduced Ti-atoms[21, 22], but for simplicity, the notation above is used. The possibility of Frenkel defects are omitted because of the close packed structure. The A-site deficiency is also omitted from the charge carrier density calculation below because of the $\left(V_{Sr}''V_O^{\bullet\bullet}\right)$-association, which is not considered to contribute to the charge carrier density. The charge carrier density of the stoichiometry $(La_{0.12}Sr_{0.88})_{0.95}TiO_{3-\partial}$ can then be estimated by the following equation

$$n = \frac{\left(0.12 \cdot 0.95 + 2 \cdot (\partial - 0.05)\right) \cdot N_A \cdot \rho}{M_m} \tag{2.19}$$

Where N_A is Avogadro's number, ρ is the material density and M_m is the molar mass of the stoichiometry. From this equation, it becomes clear that the reduction level ∂ of the material have a significant impact on the charge carrier density of the material.

2.3 Electrical conductivity

The electrical conductivity of a sample is, just like thermal conductivity, the rate at which an electric current may pass through the material.

$$\sigma = ne\mu \tag{2.20}$$

Where σ is the electrical conductivity often given in S/cm, n is the charge carrier concentration, e is the electron charge and μ is the electron mobility. This equation is slightly simplified, as it does not include minority charge carriers.

2.3.1 Electron mobility

The electron mobility is determined by[23]

$$\mu = \frac{e\bar{t}}{m^*} \tag{2.21}$$

Where $\bar{t}$ is the mean time between scattering events and m^* is the effective charge carrier mass. It becomes obvious that the large effective mass of the material also has some detrimental effect on the electron mobility. This high charge carrier mass is however still wanted, because the Seebeck coefficient is squared in the figure of merit, and thereby have a bigger impact on the figure of merit.

2.3.2 Reduction level

As explained in section 2.2, the charge carrier density, or n is heavily impacted by the amount of reduction in the sample. For each oxygen that is removed from the lattice in a reducing atmosphere, two charge carriers will be introduced to the sample. The reduction of the Ti-atoms from oxidation state +4 to +3 to compensate for doping and reduction of oxygen content, suggests localized charge carriers instead of carriers contributed to a conduction band, since the electrical conductivity increase with temperature[22]. The main reason for the increase with temperature is an improved mobility with higher temperature. The reduction level is also the easiest material parameter to manipulate, after sintering, to achieve a good electrical conductivity.

2.3.3 Electron transport

The electrons in the material do not contribute to a conduction band the same way a metal would because the bands in perovskites are narrow and do not create a single conduction band. The main charge transport is the Ti-atoms of different oxidation states allowing polaron hopping between them. The reduced Ti-atoms has an empty state, where electrons can temporarily reside[17]. It is thereby possible for electrons to move through the reduced B-sites by using oxygen bridges in between, as shown in Figure 2.7[17].

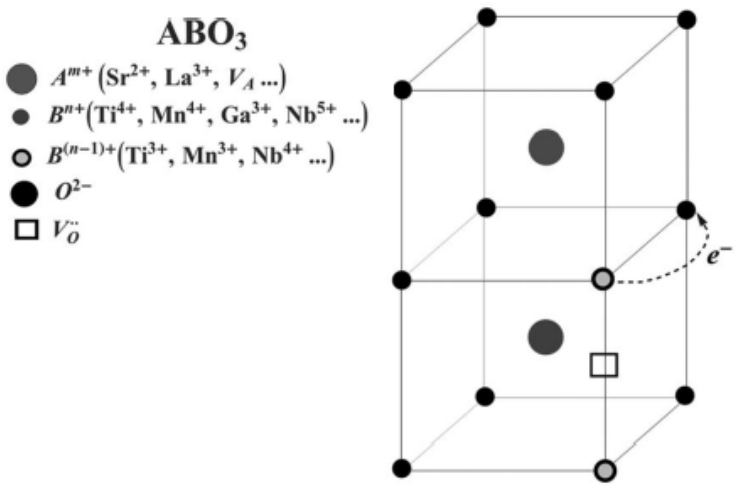

Figure 2.7: A schematic representation of the electron conduction between Ti-ions of different oxidation states[17]. The oxygen atoms have been removed for clarity.

There is a possibility for conduction between singly ionized oxygen vacancies as well[24], but polaron hopping on the reduced B-site is considered the most important mode of electron transport.

2.4 Thermal conductivity

The thermal conductivity for any given material is the rate of which heat energy travel through the material. A higher thermal conductivity will allow heat to travel more easily through the material and will result in thermal gradients, over the scope of the sample, to equilibrate. For thermoelectric purposes, a low thermal conductivity is favored, since a high thermal gradient is wanted. This can also be seen from the definition of the thermoelectric figure of merit shown in equation (2.10). Heat is quantified vibrations, when in the material lattice, they are often called phonons. It is possible to model these as waves traveling through the material. Obstructions in their path will cause scattering and deflect the wave from following a direct path. The same effect can be seen for light waves if one considers a translucent piece of glass. The more often this scattering happens, the longer time is required for the wave energy to reach the other end of the sample, and hence a low thermal conductivity. Kittel[25] expressed the flux of heat in a material as

$$j_U = -\kappa \frac{dT}{dx} \tag{2.22}$$

Where j_U is the flux of thermal energy, κ is the thermal conductivity and dT/dx is the temperature gradient along x-direction. It is also from this formula deduced, that a lower thermal conductivity will decrease the heat flux going through the material.

2.4.1 Contributions to thermal conductivity

The lattice contribution to the thermal conductivity is expressed as[2]

$$\kappa_{lattice} = \sum_j \int C_j(\omega) v_j^2(\omega) \tau_j(\omega) dx \tag{2.23}$$

$$x = \frac{\hbar \omega}{k_B T} \tag{2.24}$$

Where $C_j(\omega)$ is the contribution to the specific heat per frequency interval, $v_j(\omega)$ is the phonon velocity for an angular frequency ω and $\tau_j(\omega)$ is the frequency dependent phonon relaxation time, which is related to the mean free path(ℓ) as $\ell = v\tau$. This is the mean distance between scattering events. This distance is influenced by several means. Among others, impurities/irregularities or small particles introduced into the material, will cause a certain degree of phonon scattering. Also, x is the dimensionless angular frequency of phonon with $\hbar$ being the reduced Planck constant, k_B the Boltzmann constant and T being the temperature. The phonon relaxation time is the sum of all scattering rates affecting the phonons[26]

$$\tau_j^{-1} = \tau_{pp}^{-1} + \tau_{pd}^{-1} + \tau_{ump}^{-1} \tag{2.25}$$

Where τ_{pp}^{-1} is the phonon-phonon interaction rate, τ_{pd}^{-1} is the point defect scattering rate and τ_{ump}^{-1} is the Umklapp phonon-phonon interaction rate. The point defect scattering becomes less important with higher temperatures and the conductivity will decrease as phonon-phonon interactions begin to dominate. It is well known in physics that high frequency waves contain more energy, and in this case reflect a higher temperature. As the amount of phonons present in the material increases with temperature by necessity for transmitting more heat energy, the phonon-phonon scattering process will happen more often when temperatures increase. At high temperatures, this process often completely dominate all other lattice contributions and the mean free path, becomes proportional to the reciprocal temperature[25]. As the frequency of two waves increase, the probability of interaction between them will also increase, reducing the speed of heat propagation for each scattering event.

The thermal conductivity is also affected by a charge carrier contribution that is strongly related to the electrical conductivity of the material. The total conductivity is described as[26]

$$\kappa = \kappa_e + \kappa_{lattice} \tag{2.26}$$

Where κ is the total thermal conductivity of the sample, κ_e is the thermal conductivity contribution from charge carriers and $\kappa_{lattice}$ is the lattice-, or phonon-, contribution to the thermal conductivity. As has been indicated in theory about the Thomson effect, electrons are also capable of transporting heat in a material. The charge carrier contribution to the thermal conductivity is determined by the Wiedemann-Franz's law[27]

$$\kappa_e = L_0 \sigma T \tag{2.27}$$

Where L_0 is the Lorentz number, σ is the electrical conductivity and T is the process temperature. Even if the Lorentz number is considered relatively constant for metals, it may vary a somewhat in semiconductors[28].

2.4.2 Doping and imperfections

The chosen stoichiometry, and level of reduction, has some impact on the thermal properties of the sample. Inserting a heavy element like Lanthanum, will create locations in the material that can conserve a lot of wave momentum($p = mv$)[25], but is marginally affected by incoming waves with low energy. These elements then act as scattering centers that are reflecting the approaching waves, reducing conductivity. When introducing vacancies or distortions to a material, point defects are created that can scatter traveling phonons. If the material is heavily reduced, however, the charge carrier contribution in equation (2.27) will increase the thermal conductivity of the material, opposing this defect scattering. Particle exsolutions and

grain boundaries in materials will also act as phonon scattering centers. A reduction in thermal conductivity is expected for exsolutions introduced to the inside of a grain, disrupting the regularity of a crystallite. Reducing the grain size of the material will also have a significant effect on the thermal conductivity of the material. The reason for this is mainly the increased occurrence of grain boundaries that affects the phonon density of states. The reduced grain size will however also give a decreased surface-to-volume ratio, which affects the intensity of different phonon frequencies[29]. These changes in the frequency distribution will also affect the thermodynamic properties if the size is sufficiently small[29].

2.4.3 Pores

How porous a material is, can have an effect on its thermal conductivity. The porosity of the sintered material is therefore important to consider while determining the thermal conductivity. A highly porous material can decrease thermal conductivity significantly at lower temperatures. This effect is understood in that a pore represents a large defect that will scatter phonons. There have been several attempts to create a model that sufficiently describe the effect of pores on the thermal conductivity of a material[30]. By assuming closed spherical pores, Schulz proposed a model that is valid for materials with low porosity ($V_c \leq 10\%$)[30]

$$\kappa_{eff} = \kappa_0 \left(1 - V_c\right)^{1,5} \tag{2.28}$$

Where κ_{eff} is the effective thermal conductivity, and κ_0 is the thermal conductivity for the completely dense matrix material, as found in earlier sections. Having pores in your material will cause the phonons to scatter, as conduction cannot occur inside a pore. Heat transport inside pores mainly consist of radiative energy transfer. The rate of such energy transfer is determined by the Stefan-Boltzmann equation

$$Q = \varepsilon \sigma T^4 \tag{2.29}$$

Where Q is the rate of heat transfer in W/m^2, ε is the emissivity of the material and σ is the Stefan-Boltzmann constant which has a value of $5.670 \times 10^{-8} Wm^{-2}K^{-4}$. It can be seen from the equation, since σ is quite small, that this type of energy transfer is negligible at lower temperatures. However, as high temperatures will cause more heat to be transported in pores, an incorporation of temperature into the calculation of the thermal conductivity of the material is necessary. Having temperature as a variable, a modified Loeb's formula was proposed from measurements performed on unirradiated UO_2 fuel[30]

$$\kappa_{eff} = \kappa_0 \left(1 - \eta V_c\right) \tag{2.30}$$

Where η is an empirical parameter expressed as a function of temperature (°C), where $\eta = 2.6 - 0.5 \times 10^{-5} T$. This empirical parameter may differ some between

different systems, and has for another system been found to be $\eta = -0.1 + 6.9\times10^{-3}T - 3.7\times10^{-6}T^2$ [30]. Pore size is also a parameter that have some impact on how much radiative energy is transferred inside pores, however because the temperatures in this study mostly lie at or below 800°C this will not be further elaborated in this report.

2.5 Spark Plasma Sintering (SPS)

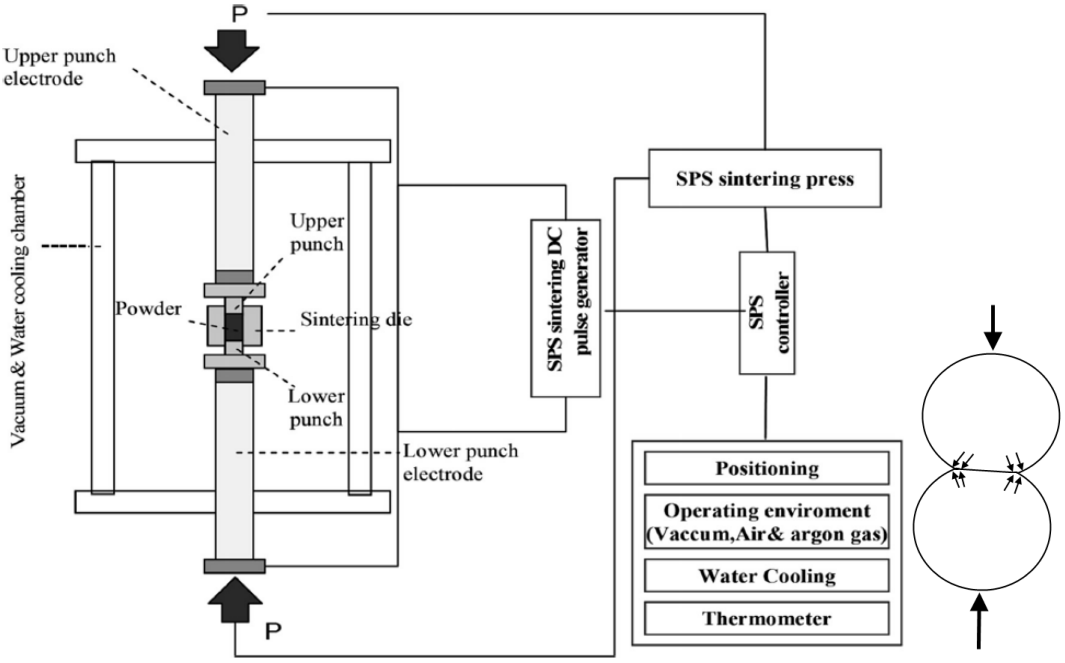

Figure 2.8: Left: A schematic representation of the SPS process [31]. Right: A schematic showing the pressure applied and small arrows in the direction toward which the grains will grow.

Spark plasma sintering is a sintering technique that requires significantly less time to sinter a sample than conventional sintering. Conventional sintering typically runs for several hours while SPS only need a few minutes to achieve a high-density sintered material. In conventional sintering a sample is typically pressed before sintering and heated in an oven. The heat will cause the necking formation that is the basis for the sintering process. If one is to achieve a sintered sample in a reasonable amount of time with this method, high temperatures is required to speed up the material diffusion. Having unreasonably high temperatures will however have the adverse effect of significant grain growth. For some materials, this may not be a problem, but if the thermal conductivity is to be kept low, grain growth is unfavorable. This is where Field Assisted Sintering Technology(FAST), here represented by the SPS process, comes into play. It is possible to introduce other fields to aid in sintering than only heat. Pressure and electricity can be added to aid the sintering process. For the hot press sintering technique, which is also a FAST-technology, only pressure is applied in addition to heating, which give a significant reduction in required sintering time. The temperature required is however still high. The Spark Plasma Sintering technique also introduces electrical current to the system to aid in sintering. A high

voltage current is applied and will be conducted mostly along the surfaces of the powder particles. At locations where particles create a possible path for electricity, i.e. is touching, a localized heating will occur where the electrical resistance is highest, i.e. the contact points between particles. Since most of the sample heating is strongly localized, only small amounts of grain growth is displayed from materials processed with this sintering method.

3 Literature review

3.1 Non-oxide material

Materials that show the highest values of figure of merit are typically non-oxides at present day. Some of these materials are however composed of expensive heavy metals such as Bi and Pb, which are also not favorable with respect to the environment[7].

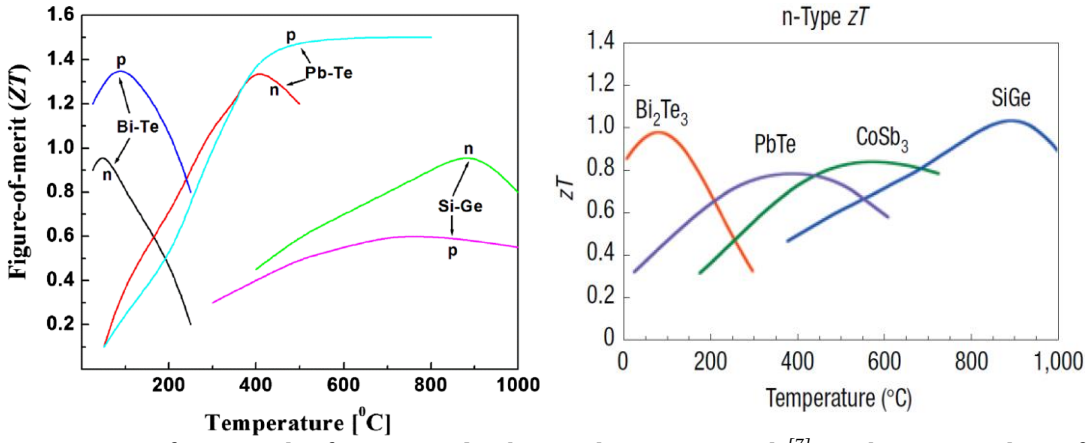

Figure 3.1: Left: ZT-vaules for non-oxidic thermoelectric materials[7]. Right: Some values of ZT reported for n-type thermoelectric materials that are not oxide materials[32].

As can be seen from the graphs presented in Figure 3.1, the figure of merit of various non-oxide materials are quite decent. For high temperature applications, however, oxides are favored in part because of their structural and chemical stability[7]. This will allow for a high thermal gradient over the material and hence a high Carnot efficiency, which to some degree compensate a low figure of merit[6].

3.2 Oxide materials

As oxide materials have shown potential to be able to become the next step for high-temperature thermoelectric devices, much effort is put into finding material properties that maximize its potential as a thermoelectric material.

3.2.1 State of the art

Three oxide material systems are thoroughly investigated for n-type thermoelectric behavior. These are materials based on ZnO, $CaMnO_3$ and $SrTiO_3$[8]. ZnO material with varying doping strategies hold promise for good high temperature thermoelectric material. The electrical and thermal conductivities do however change a lot with grain size in this material[8]. The material do however display a good electrical conductivity that is maintained somewhat better to higher temperatures than i.e. $SrTiO_3$ materials[8]. $CaMnO_3$ material generally have both a lower thermal and electrical conductivity than $SrTiO_3$-type material, but some intricate doping is still able to display decent properties[8]. There are several other material that have been investigated[6], but the $SrTiO_3$ system is along with the ZnO system probably the most promising candidates for good n-type thermoelectric oxide material[6].

3.2.2 $SrTiO_3$ materials

According to Dang et al.[33] heavily doped Strontium Titanate(STO) is a promising n-type thermoelectric material because of a large effective electron mass in the order of 6 to 15 times that of the electron rest mass. The authors have previously gained a figure of merit of 0.08 at 300 K for La-doped $SrTiO_3$. The same material had an electrical conductivity of 1000 S/cm and a Seebeck coefficient of -150 µV/K. With a Nb-doped epitaxial film of STO the team was able to attain a figure of merit of 0.37 at 1000 K. Further, the same team also found a Nb-STO/STO superlattice to exhibit a massive Seebeck coefficient that gave a figure of merit of 2.4 for a one unit cell thick Nb-STO layer, which is claimed to be because of the formation of a two-dimensional electron gas. The team suggests that the lowering of the thermal conductivity in bulk STO, which the team found to be about 11 W/mK, might be important to further increase its figure of merit. The team also points out an analysis where Kapitza resistance at grain boundaries where the grain size is 10 nm suggested that thermal conductivities down to 2 W/mK at 300 K may be possible in a nanoceramics.

3.3 Nanostructuring

By reducing the size of the material that is to be sintered, diffusion lengths in the material will become small, and a phase pure material is easier to achieve[34]. By nanostructuring the material, a lower calcination temperature[34], and potentially sintering temperature can be used. The increased surface-to-volume ratio increase all reaction rates[29]. The nanostructuring of the material can be done in several ways[29]. As this work is a continuation of the work of Loland[35], the powder was already synthesized using the spray pyrolysis process. This material exhibited a grain size of roughly 20nm, which is a good starting point. Koumoto et al.[36] reported an almost linear reduction in thermal conductivity with grain sizes down from 100 nm. The team also found a phonon mean free path of about 1.15 nm for a 55nm grain size as opposed to 1.6nm for a sample with a grain size of 10 µm.

3.4 A-site deficiency and TiO_2 exsolution

Several reports have been published concerning A-site deficient Lanthanum-doped Strontium Titanate[16, 34, 37]. An important trait of this deficiency is the possibility of exsolution of a TiO_2-phase[18]. This type of exsolutions is particularly interesting if it should prove possible to introduce them on the inside of a grain. By doing this, the mean free path of phonons could be significantly reduced by interrupting its path going through the grain, and reducing thermal conductivity. The reduced phase without TiO_2 exsolutions does however seem to exhibit a remarkably higher electrical conductivity than more stoichiometric material with as high as 600 Scm^{-1} at 600 °C[16].

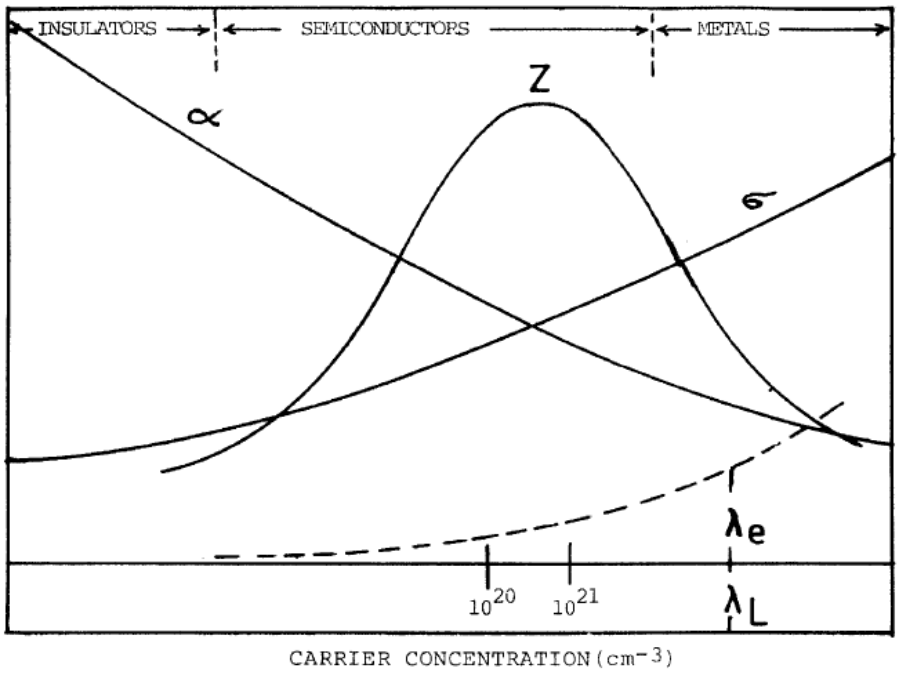

Figure 3.2: The charge carrier concentration dependence of the different thermoelectric parameters [38]. Here α is the Seebeck coefficient, Z is the temperature independent figure of merit, σ is the electrical conductivity and λ_e and λ_L is the charge carrier and lattice contributions to the thermal conductivity respectively.

3.5 Charge carrier dependence

The amount of charge carriers impact all three parameters that are important for thermoelectric applications, as can be seen in Figure 3.2. A compromise between these must therefore be done in order to maximize the figure of merit. The Seebeck coefficient is strongly related to the electrical conductivity of the sample through the charge carrier concentration and the effective mass of these. One of the reasons why STO has become a popular thermoelectric material is the large effective mass of electrons in this material[2]. The optimum charge carrier concentration for a thermoelectric semiconductor material typically lies between 10^{20} and 10^{21} cm^{-3}[38], but there are some differences depending on the material.

4 Experimental

4.1 Chemicals and Apparatus

The powder that were used in sample sintering was taken from previous work with the same stoichiometry[35]. This powder was created in cooperation with Ceramic Powder Technology AS in Trondheim using the spray pyrolysis process. From the process, the powder was not calcined or milled. This was performed by Loland in his specialization project. The powder was calcined at 600°C to minimize grain growth and subsequently wet milled in 96% Ethanol before drying the powder and sieving with a 250 µm sieve.

Table 4.1: List of chemicals used in the experimental work.

Chemical	Supplier	Purity (%)
Isopropanol	VWR International AS	>99.8%
Nitrogen gas	Yara Praxair	$pO_2 \leq -5$

Table 4.2: The instruments used in the experimental work and their model names.

Use	Model
X-ray diffraction	Bruker D8 Advance DaVinci X-Ray Diffractometer
Dilatometry	NETZSCH DIL 402C
Archimedes' measurement	Home built apparatus
Spark Plasma Sintering	Dr Sinter 2050 SPS
Scanning electron microscopy	Zeiss Supra 55 VP
Transmission electron microscopy	Jeol ARM200F
Measure electrical conductivity	Home built 4-point probe design
Seebeck measurement	NorECs Probostat™
Thermal conductivity measurement	Netzsch LFA 457 MicroFlash

4.2 Procedures

In order to increase the reproducibility of the measurements performed in this work, a section concerning how the experimental work was performed is included.

4.2.1 Sample names

The sample names are named according to the following pattern:

$$[\text{Sintering temperature}]\_[\text{Pressure}]\_[\text{Holding time}]\_[\text{Sample nr.}]\_[\text{Batch}]$$

The sintering temperatures ranges from 900°C to 1200°C. The pressure is mostly kept at 50MPa, but three samples have different pressure during sintering. For the work presented in this thesis all samples were kept for 5 minutes in the sintering oven. The sample number is to identify the different samples with the same sintering parameters. The batch marker relates to different batches of the sintered powder from spray pyrolysis. The powder samples was formerly produced by Loland[35]. The naming convention used for these batches by Loland follow this pattern:

$$[\text{Dilution}]\_[\text{Flow rate}]\_[\text{Cyclone}]$$

Dilution represents the degree of dilution of the precursor solution used in the spray pyrolysis. Flow rates used was set either to a high rate or at a low rate, since no flow meter was installed. The processing facility had two sample collecting cyclones. The big cyclone (B) collected most of the sample, while the smaller one that was connected later in the air stream collected some of the powder that escaped the big cyclone.

Table 4.3: The connection between the batch names used by Loland[35] and the samples in this work.

Batch	Names from Loland[35]
A	C2_HI_B
B	CM_HI_B
C	CM_LO_B

A table explaining all samples will be included in the appendix.

4.2.2 Sample preparation

In order to fit the apparatuses used for characterization, the samples had to be cut to shape. The electrical conductivity measurements and Seebeck apparatus could both be operated with samples that had a height and width of approximately 3mm, while the length was typically the diameter of the SPS sample (20mm). Also the Thermal Flash analysis needed samples of a particular size and shape. These needed to be circular and have a diameter of approximately 0.5" to fit the sample holder. This cutting proved a challenge due to the brittleness of the samples, and several samples were destroyed during cutting. The cutting was performed by professionals.

The samples prepared for x-ray diffraction was mortared from a piece of sintered sample in order to avoid local effects from the pellet surface.

4.2.3 Archimedes density measurement

In the Archimedes method, a sample is weighed when it is dry, when it is submerged in isopropanol and while wet with isopropanol but above the surface. Before submerging the samples in isopropanol, the samples were introduced to a chamber with a vacuum. This was done in order for the isopropanol to be able to enter all the open pores with ease. The measured weights was used to determine the material density and porosity. The temperature of the isopropanol was also recorded. This temperature is required to determine the density of the isopropanol. The two simple formulas below is used to attain the material density and porosity.

$$\text{Open porosity} = \frac{m_c - m_a}{m_c - m_b} \cdot 100\% \tag{4.1}$$

$$\rho_{sample} = \frac{m_a}{m_c - m_b} \cdot \rho_{isopropanol} \tag{4.2}$$

Where m_a is the mass of the dry sample in air, m_b is the mass of the wet sample submerged, m_c is the mass of the wet sample in air and $\rho_{isopropanol}$ and ρ_{sample} are the densities of isopropanol and the sample material, respectively. It is also possible to get the closed porosity of the sample.

4.2.4 4-probe conductivity measurement

The four-probe measuring technique was used in order to measure the electrical conductivity of the samples. The apparatus is of a home built design, which is schematically represented in Figure 4.1.

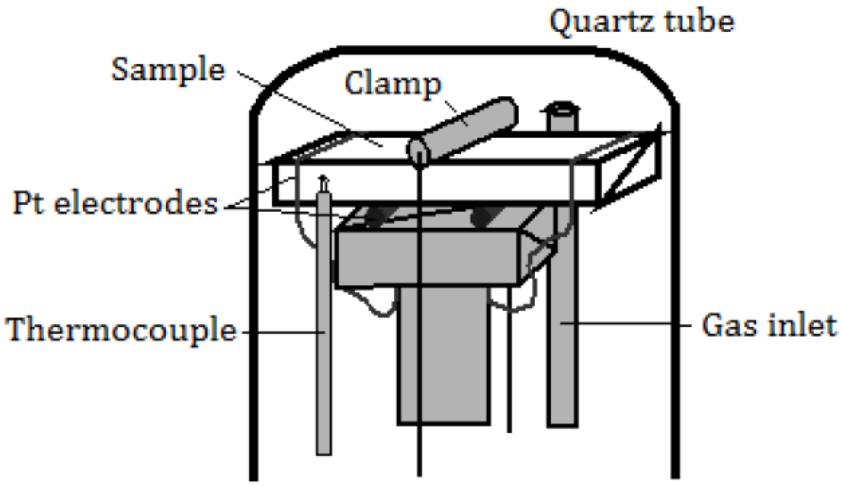

Figure 4.1: A schematic representation of the 4-probe conductivity measurement device[1].

In this method, two wires apply an electrical current to the sample, while two wires measure the potential drop measured over a given length of sample. With the known cross section area of the sample and assuming a homogeneous conductivity in the sample, the conductivity is calculated by

$$\sigma = \frac{I}{U} \cdot \frac{\ell}{A} \tag{4.3}$$

Where σ is the electrical conductivity, U is the potential drop in the sample, I is the current through the sample, ℓ is the length of the sample and A is the cross sectional area of the sample.

The electrical conductivities were measured in a Nitrogen atmosphere. Because of some instrumental difficulties, the flow rate in the system was higher than 50 mL/min, which was the target. To ensure a decent contact between the sample and the platinum wires, a platinum paint was also applied in the contact points. Two different temperature programs were followed in the measurements of electrical conductivity. The first measurements were taken with only a 200°C/h heating rate and holding the sample at the top value for some time. These samples exhibited somewhat higher electrical conductivity since they did not have the same amount of time to oxidize. Since these samples probably are not at thermal equilibrium while heating up, the values from these measurements are not included.

Table 4.4: The temperature program used in the 4-probe measurement oven.

Start Temperature (°C)	Ramp-rate (°C/h)	Stop Temperature (°C)	Holding time (h)
26	100	200	3
200	100	400	3
400	100	600	3
600	100	700	3
700	100	600	3
600	100	400	3
400	100	200	3
200	200	26	-

4.2.5 Thermal Flash analysis

The thermal conductivity of the samples were determined by using the Netzsch LFA 457 MicroFlash, which is sketched below.

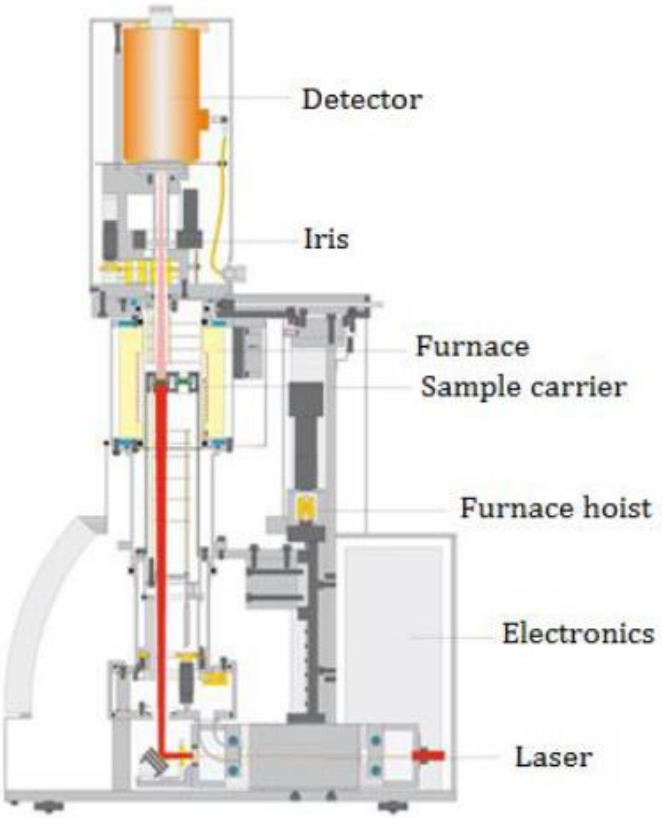

Figure 4.2: A schematic representation of the Laser Flash device that was used for determining the thermal properties of the samples[1].

The Laser flash measurements determine the thermal diffusivity and heat capacity of the material, which can be used in order to determine the thermal conductivity of the sample through the formula

$$\kappa = \alpha \cdot \rho \cdot C_p \tag{4.4}$$

Where κ is the thermal conductivity, α is the thermal diffusivity, ρ is the density of the material and C_p is the material specific heat. The samples are coated with graphite before being placed into the apparatus. This is done to ensure a high degree of absorption on the surfaces. By flashing a laser pulse on one side of the sample and measuring the time it takes for the heat to get through the sample, it is possible to determine its thermal diffusivity and the specific heat. The samples were measured in the interval between room temperature and 800 °C, with three recordings performed for each 100 °C, in a N_2-atmosphere and a flow rate of 50 mL/min.

4.2.6 Seebeck coefficient measurements

The Seebeck coefficient measurements were performed with a Probostat device from NorECs AS. The part that is inserted into a temperature gradient is sketched in Figure 4.3. A N_2-atmosphere was used, with a flow rate of 50 mL/min.

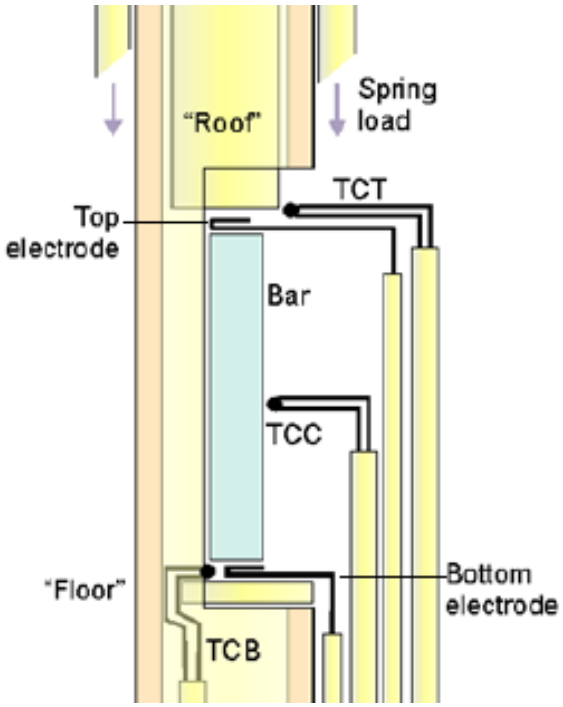

Figure 4.3: A schematic representation of the device that was used in determining the Seebeck coefficient of the samples[1].

Because of some experimental errors, the temperature difference between the top and bottom part were measured incorrectly for some samples. The placement of the sample in the oven was however roughly the same. The incorrect temperatures of the given samples are therefore substituted by a more correct temperature difference from the sample 1050_50_5_S3_B. Because of some difference in the thermocouples response to temperature, a calibration of these were performed in order to minimize this error in the measurements. This also introduces a certain error in the measurements. Because of the accumulated errors in these measurements,

the results should be viewed in a critical eye and considered as an approximation to the actual results.

Table 4.5: The temperature program used in Seebeck coefficient measurements.

Start Temperature (°C)	Ramp-rate (°C/h)	Stop Temperature (°C)	Holding time (h)
26	100	200	4
200	100	400	3
400	100	600	3
600	100	700	3
700	100	600	3
600	100	400	3
400	100	200	3
200	200	26	-

4.2.7 Transmission electron microscopy (TEM)

The TEM samples were investigated using a Cs probe- and image-corrected cold-FEG JEOL ARM 200F, operated at 200kV. The TEM is equipped with a Centurio silicon drift detector (0.8 sr solid angle) for EDX and Quantum GIF with DualEELS.

The TEM-sample from the sample sintered at a pressure of 50 MPa and a temperature of 1200 °C was made by tripod wedge polishing, which is described in detail by Eberg et al.[39]. The other samples were thoroughly ground in a mortar, and transferred to a carbon film, used as a substrate holder inside the TEM.

5 Results

5.1 Density and porosity

The density and porosity of the samples were determined by Archimedes' method. Densities increase with temperature because of an increased diffusion rate, as would be expected from sintering theory. The only way the necking formation, that is characteristic for the sintering process, can form is by material diffusion. From Figure 5.1 it is observed that a higher pressure will give a more densely sintered sample. This is also as expected from theory, as the pressure also will aid in compaction of the sample during the sintering process. A low relative density mean a high porosity. This porosity is however divided into open and closed porosity, where open porosity is pores exposed to the environment and closed pores are cut off from the outside.

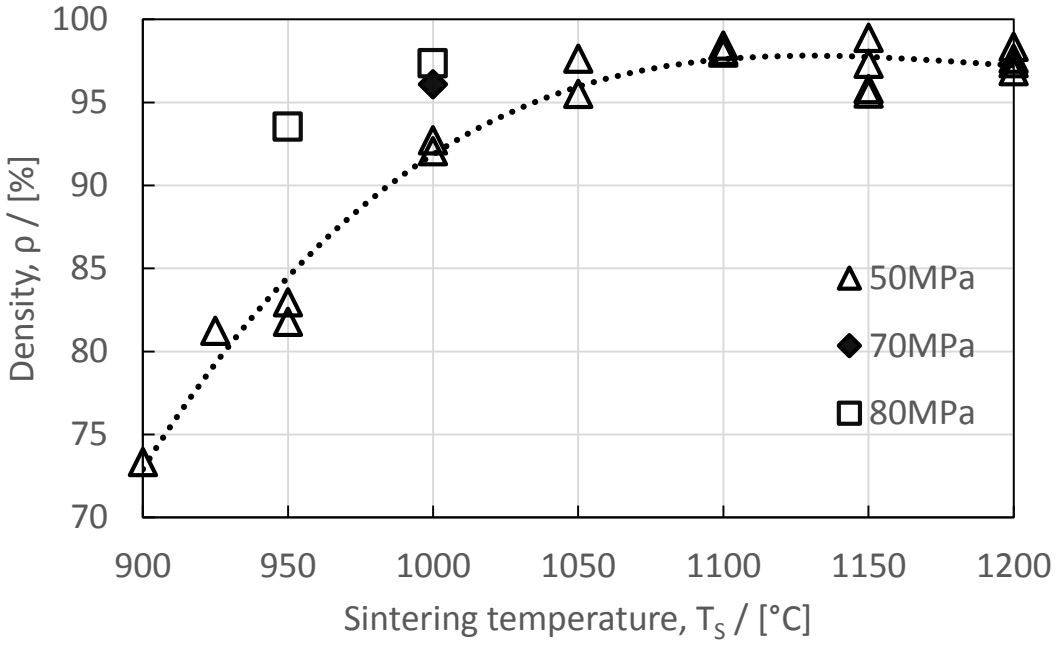

Figure 5.1: Densities of the samples as measured by Archimedes' method. Each of the samples were sintered for 5 minutes at different temperature and pressure. The dotted line is included as a guide to the eye. The theoretical density is set to 5.1595 g/cm^3, which is an approximate value since the lattice parameter is slightly different for each sample.

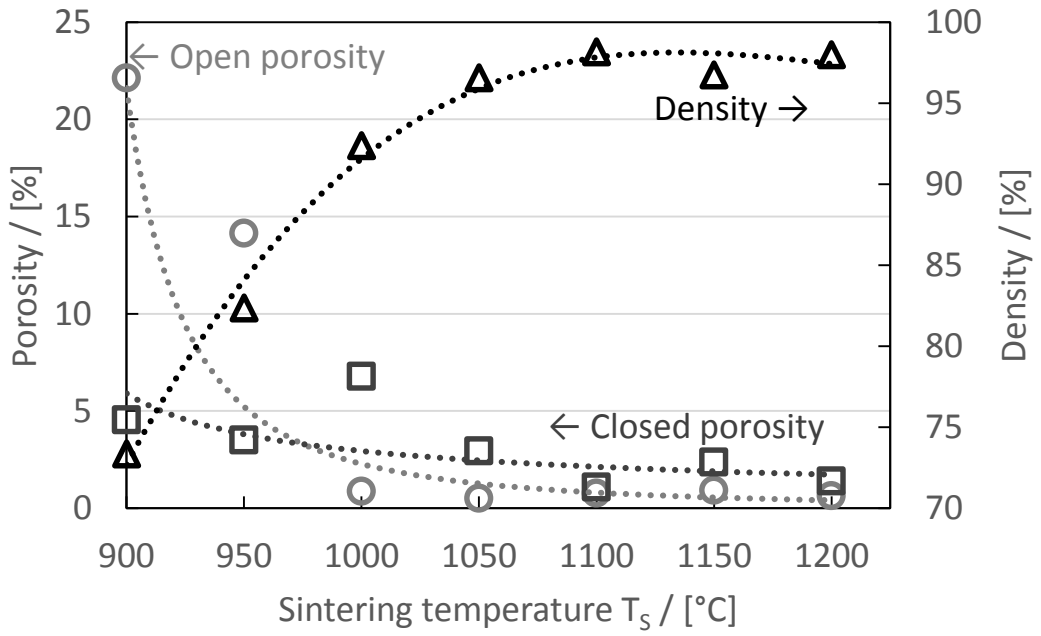

Figure 5.2: The porosity of some of the samples sintered for 5 minutes at 50MPa as determined by Archimedes' method. The dotted lines are inserted as a guide to the eye. The theoretical density is set to 5.1595 g/cm^3, which is an approximate value since the lattice parameter is slightly different for each sample.

5.2 X-ray diffraction

X-ray diffraction (XRD) is a common technique in materials science. The method relies on an incoming x-ray beam being reflected back from the material lattice. From the reflected patterns, it is possible to determine crystallographic information about the samples.

5.2.1 Crystallite size and lattice parameter

To determine the crystallite size of the samples sintered at different temperature, their X-ray diffraction (XRD) patterns were collected. The recorded diffraction patterns were subsequently introduced into a curve fitting software. A Scherrer analysis were performed on the fitted curves, which determines the crystallite sizes and the lattice parameter[40].

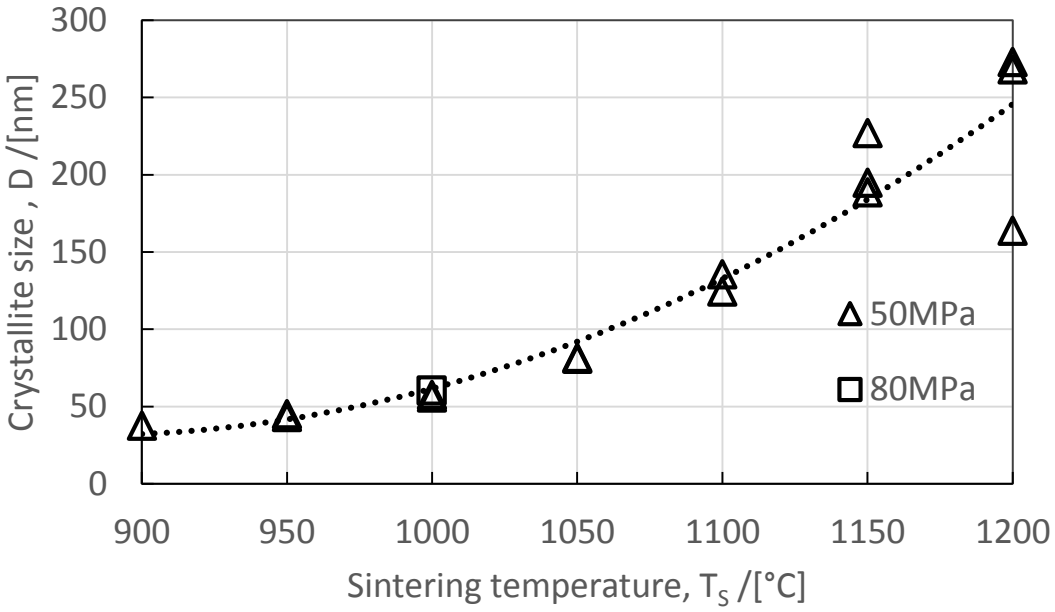

Figure 5.3: Scatter plot of crystallite sizes as calculated by the Scherrer method in the Topas software by Bruker. Note the inaccuracies at higher sintering temperatures, this is probably because of increased internal strain in the samples which distorts the XRD patterns. The dotted line is inserted as a guide to the eye.

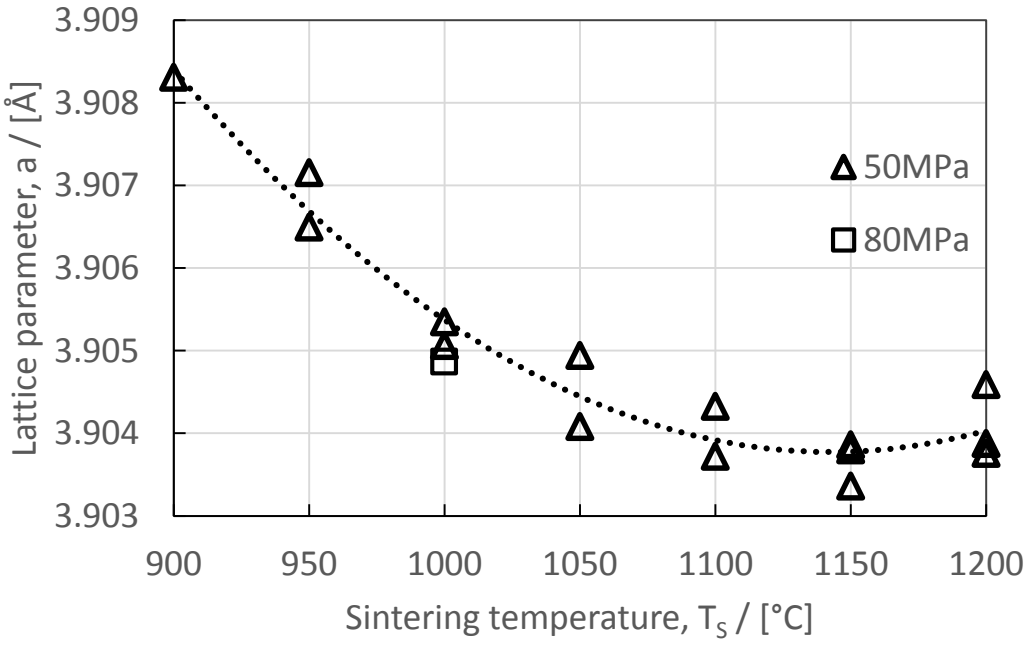

Figure 5.4: The lattice parameter of the primary phase, as determined from the XRD-plots by the use of Rietveld analysis in the Topas software. The dotted line is inserted as a guide to the eye.

5.2.2 Secondary phase

From the XRD patterns, it is possible to determine phases present in the material by reference to a database of known materials and their crystal structure. Here, the PDF database from the International Centre for Diffraction Data (ICDD) was used.

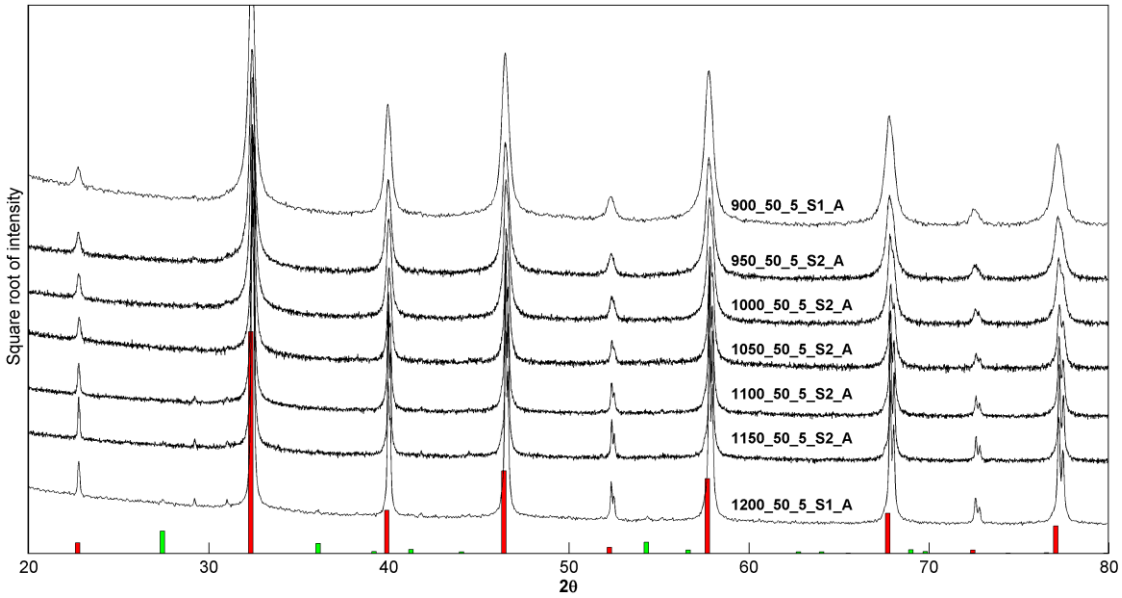

Figure 5.5: XRD scan from 20 to 80 degrees from the different temperatures. The red peaks represent $La_{0.1}Sr_{0.9}TiO_3$ with the PDF reference 04-002-1010. The green peak represent the secondary phase TiO_2 with PDF reference 04-003-0648. The x-rays were produced using a copper anode.

To determine the presence of TiO_2, a shorter scan was performed in the proximity of the most distinct peak for this phase. This peak is at approximately 27.4° 2θ. Below a sintering temperature of 1150 °C, the peak completely vanish. The peak at roughly 26.5° 2θ was found to be remnant graphite from the sintering step.

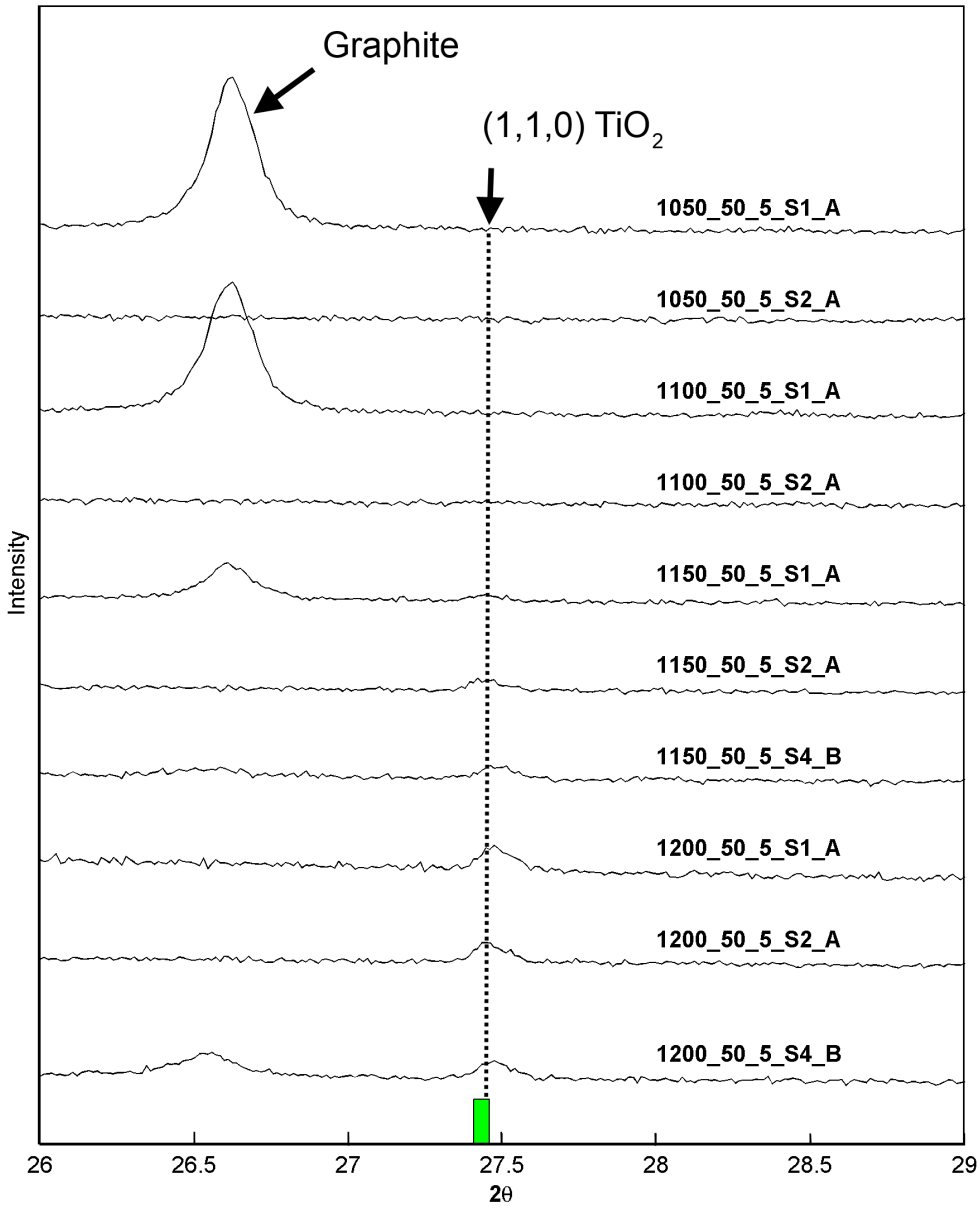

Figure 5.6: An XRD-scan to determine the presence of TiO_2 in the samples. This is measured on the most distinct peak for TiO_2 with PDF-reference 04-003-0648, which is indicated by the green bar. The peak at 26.6 represent graphite, and is caused by traces of remnant graphite from the sintering of the samples. The X-rays were produced by a copper anode.

5.3 Scanning Electron Microscope

An attempt was made to image the fracture surface of the samples by using a Scanning Electron Microscope (SEM). In order to avoid deep penetration and see most of the topography in the sample, a low accelerating voltage of 5kV was used. Even if the photos are a bit diffuse, it is clear to see that the grain size decrease quite a lot with a decrease of 100 °C in sintering temperature.

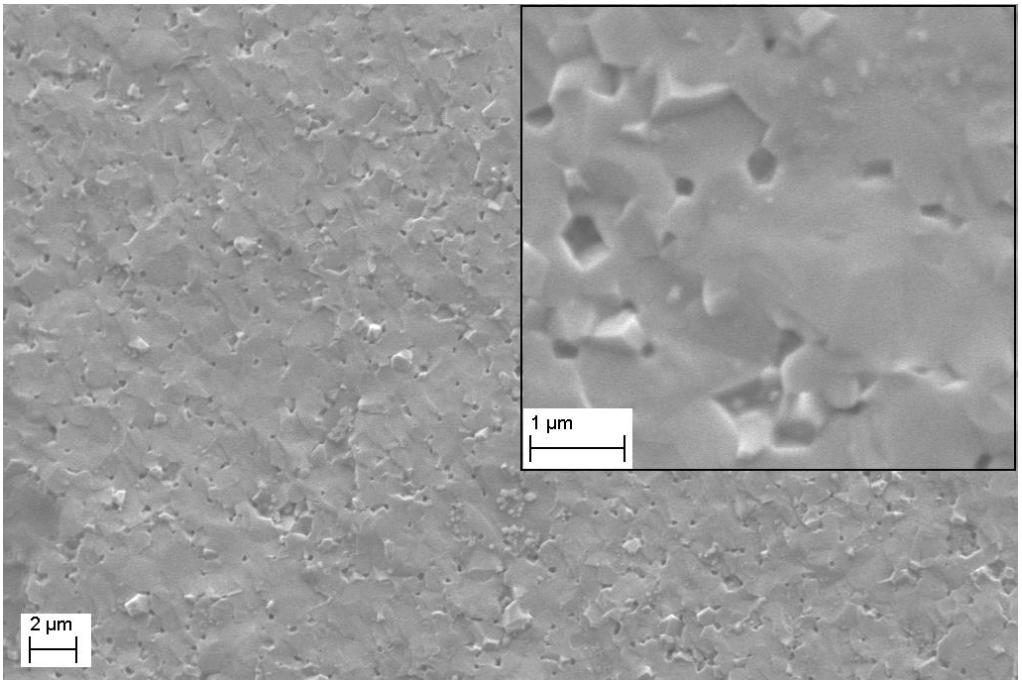

Figure 5.7: SEM photo with two different magnifications of a sample sintered at 1200°C. The image is taken in backscatter mode on a fracture surface with an accelerating voltage of 5kV.

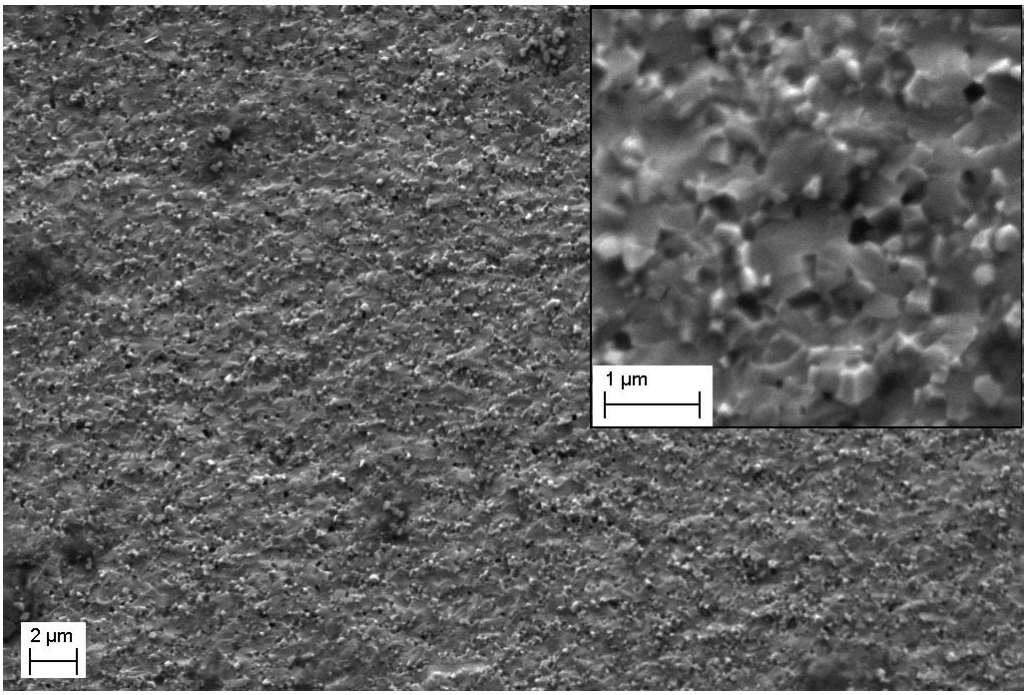

Figure 5.8: SEM photo with two different magnifications of a sample sintered at 1150°C. The image is taken in backscatter mode on a fracture surface with an accelerating voltage of 5kV.

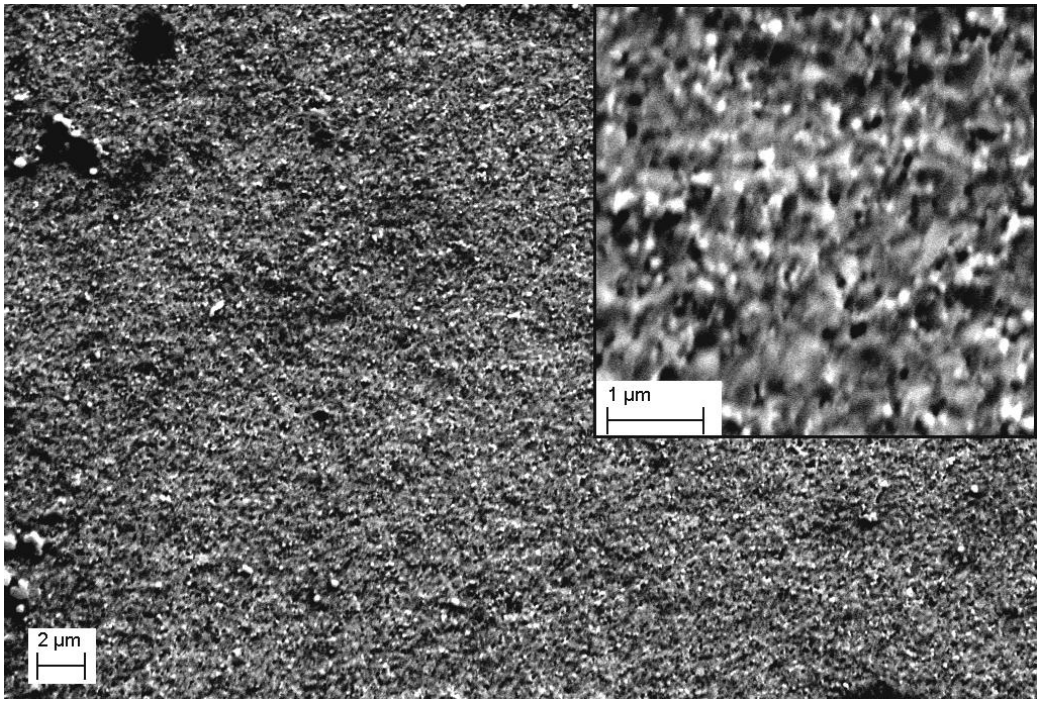

Figure 5.9: SEM photo with two different magnifications of a sample sintered at 1100°C. The image is taken in backscatter mode on a fracture surface with an accelerating voltage of 5kV.

5.4 Transmission Electron Microscope

The first attempt at recording TEM photos was performed on a mortared sample, and it is hence a bit difficult to determine the presence and locations of secondary phase etc. A small grain size was found, but the EDS mapping of the sample sintered at 950°C showed no sign of a secondary phase. In the second attempt, a sample was ground down to a thin piece of the material, to get information that is more useful. TiO_2 was found in the sample sintered at 1200 °C after this refinement. The bright dots in Figure 5.13 was found to be TiO_2 in the rutile polymorph from the diffraction patterns collected, as shown in Figure 5.14. This was verified by the EDS scans that were performed on both the primary phase and the secondary phase, as seen in Figure 5.15 and Figure 5.16.

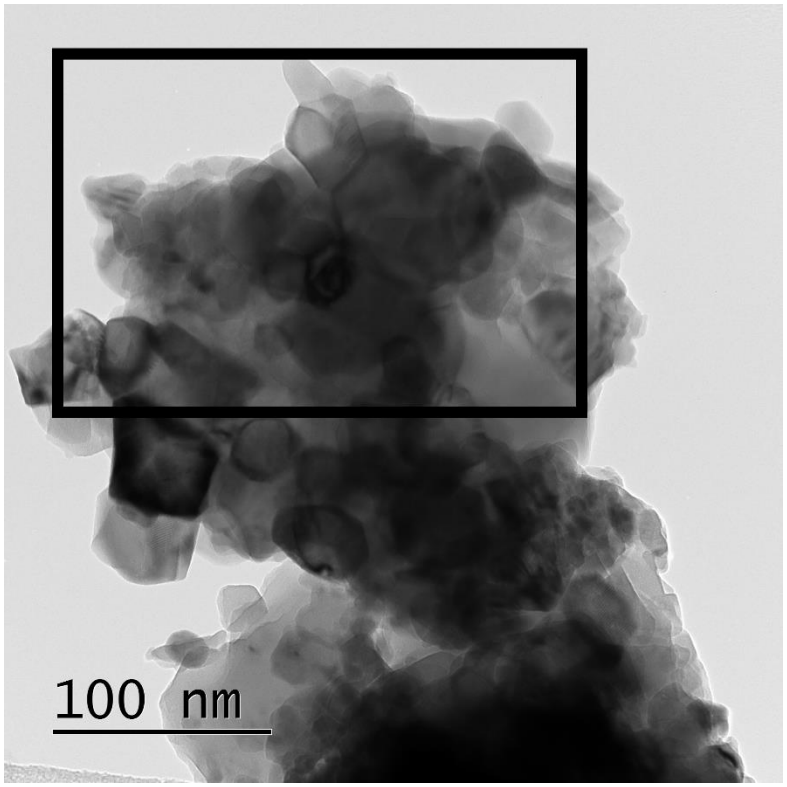

Figure 5.10: TEM bright field photo of a sample sintered at 950°C. The squared area is the approximate location that is mapped in Figure 5.11.

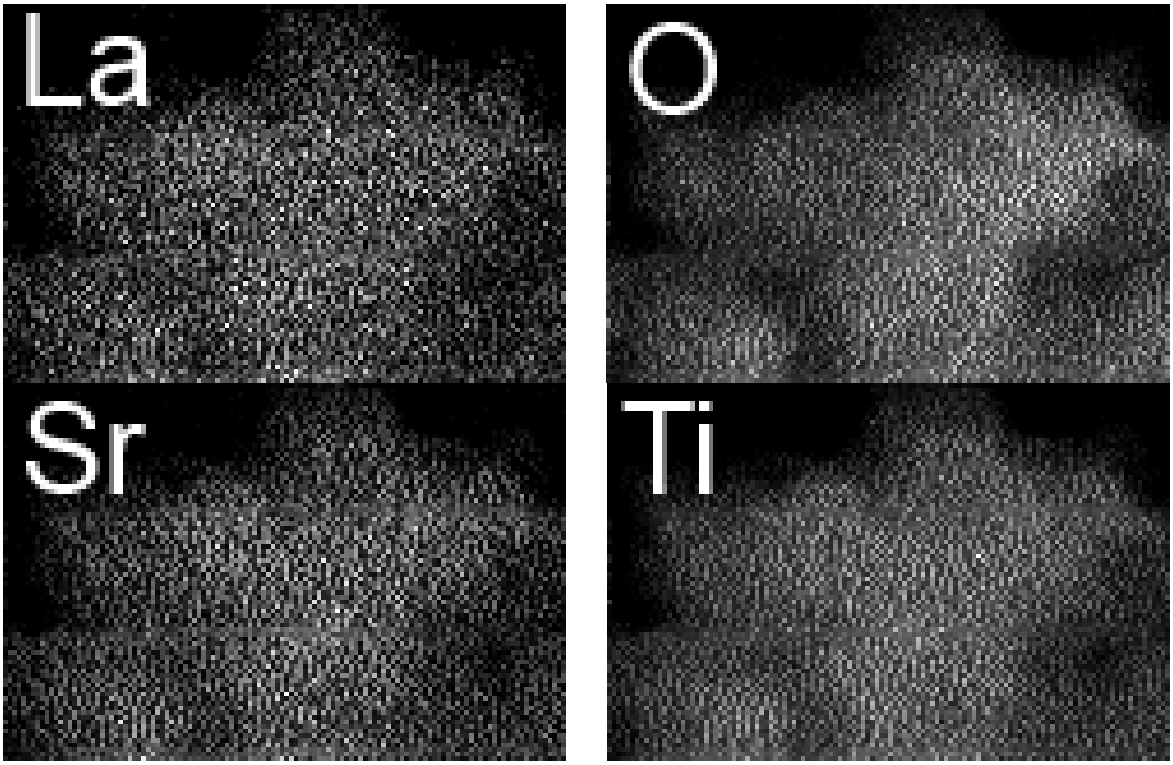

Figure 5.11: EDS mapping from the top part of Figure 5.10. Top left: Mapping of the L-peak of La. Top right: Mapping of the K-peak of Oxygen. Bottom left: Mapping of the K-peak of Sr. Bottom right: Mapping of the K-peak of Ti.

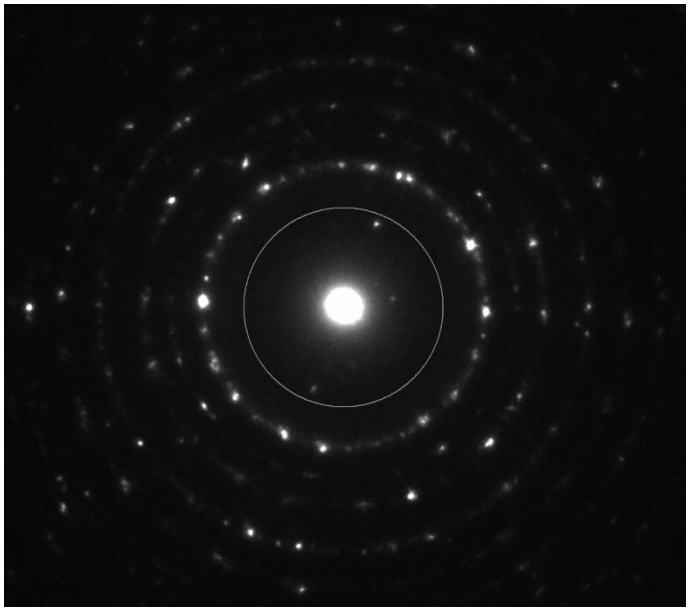

Figure 5.12: Diffraction pattern taken on the sample sintered at 950 °C. The innermost ring is not a part of the diffraction pattern. The formation of rings suggests either an amorphous material, or as in our case a nano-crystalline sample.

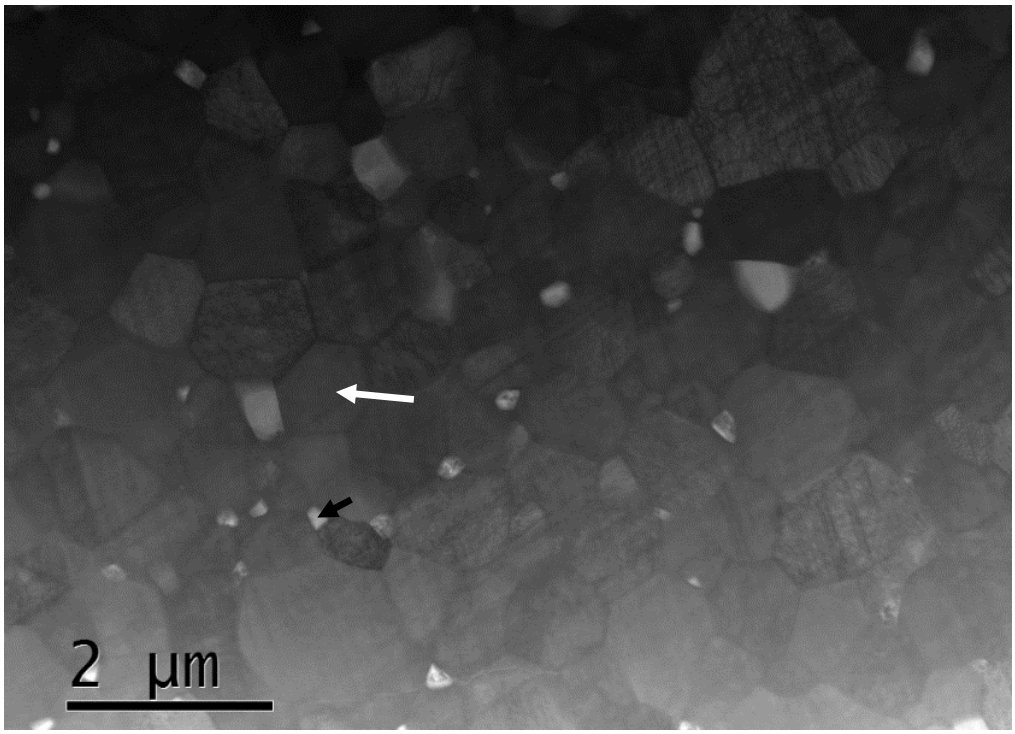

Figure 5.13: STEM photo of the sample that was wedge polished, instead of crushed, which was sintered at 1200°C. The bright particles are Rutile TiO_2. The black arrow is pointing at an area with TiO_2, while the white arrow is pointing at the primary phase.

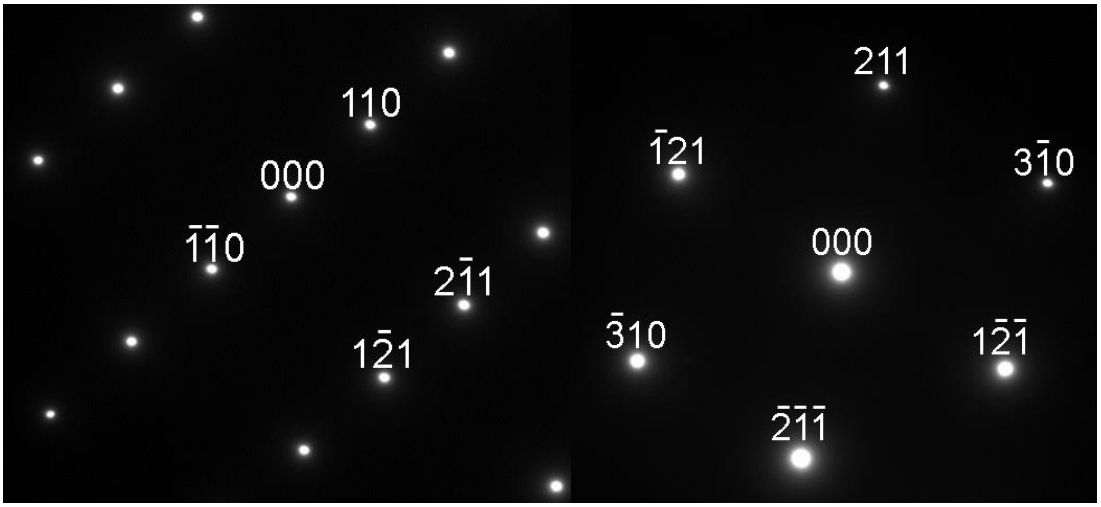

Figure 5.14: The diffraction patterns of the secondary phase obtained from two different tilting angles. The indexation is according to Rutile TiO_2, which seem to be the composition and polymorph of this phase. The diffraction patterns are collected from a point in the sample where TiO_2 was thought to reside, like at the black arrow in Figure 5.13.

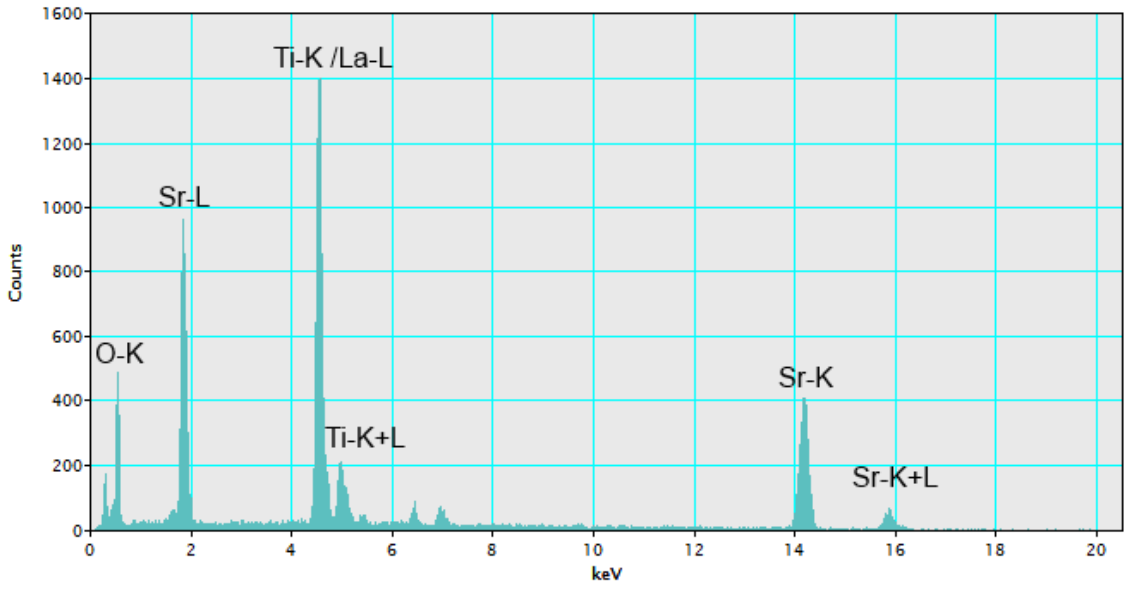

Figure 5.15: EDS scan performed in an area of the sample that was expected to be primary phase. All the elements seem to be accounted for in order for it to be the primary phase. This scan is collected from a point such as the one marked by a white arrow in Figure 5.13.

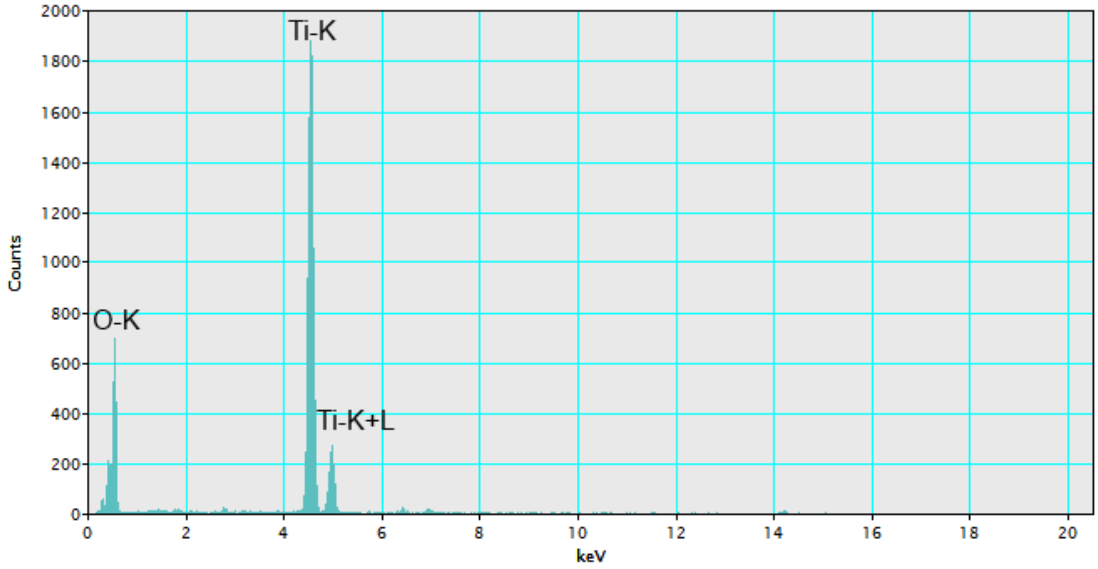

Figure 5.16: EDS scan performed in an area of the sample that was expected to be TiO_2. As seen from the indexed reflections above, only Ti and O seem to be present, which is in accordance with the diffraction patterns that was also collected. This scan is collected from a point on the sample such as the one marked by a black arrow in Figure 5.13.

5.5 Dilatometer

The samples oxidized quite a lot during the dilatometry measurements and got a pale white color. This will have some effect on the crystal structures of the samples. By knowing that the samples sintered at a lower temperature will be less reduced than the ones sintered at higher temperatures, it is possible to read the response from reduction in Figure 5.4. The sample sintered at 950 °C, however, also had much more open porosity. By having a very open porosity, oxidation happens more easily throughout the sample. Because of this bulk oxidation, the sample will display a larger expansion with temperature.

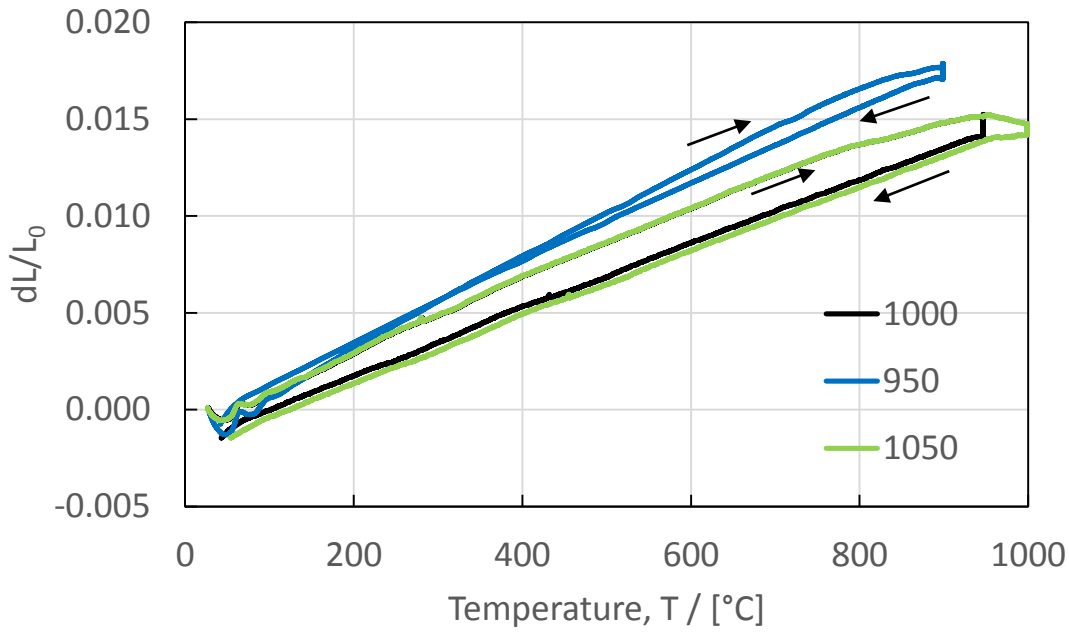

Figure 5.17: Dilatometer measurements for three of the 50MPa samples. An arrow pointing right means that the measurement is done in ascending temperature, while an arrow going left means the measurements done in descending temperature.

The thermal expansion coefficients are calculated by the measured expansion in the range between 250 °C and 150 °C, where oxidation is neglected. The formula to determine the thermal expansion is

$$\alpha_L = \frac{dL/L_0}{dT} \tag{5.1}$$

Where α_L is the linear expansion coefficient, dL/L_0 is the dimensionless expansion and dT is the temperature difference between the measuring points.

Table 5.1: Calculated thermal expansion coefficients for three of the 50MPa samples. Arrow up means before oxidation, while arrow down represent after oxidation.

Sample	Thermal expansion coefficient [$10^{-6}K^{-1}$]
950_50_5_S2_A	25.36↑ 21.84↓
1000_50_5_S2_A	20.94↑ 16.35↓
1050_50_5_S2_A	20.57↑ 18.17↓

5.6 Thermal flash

As can be seen from Figure 5.18, the thermal conductivity of the samples with a lower density and crystallite size are significantly lower than the samples that have a bigger grain size and higher density. The samples that are sintered at the lowest temperatures, which also have a low density, have a small increase in thermal conductivity at higher temperatures.

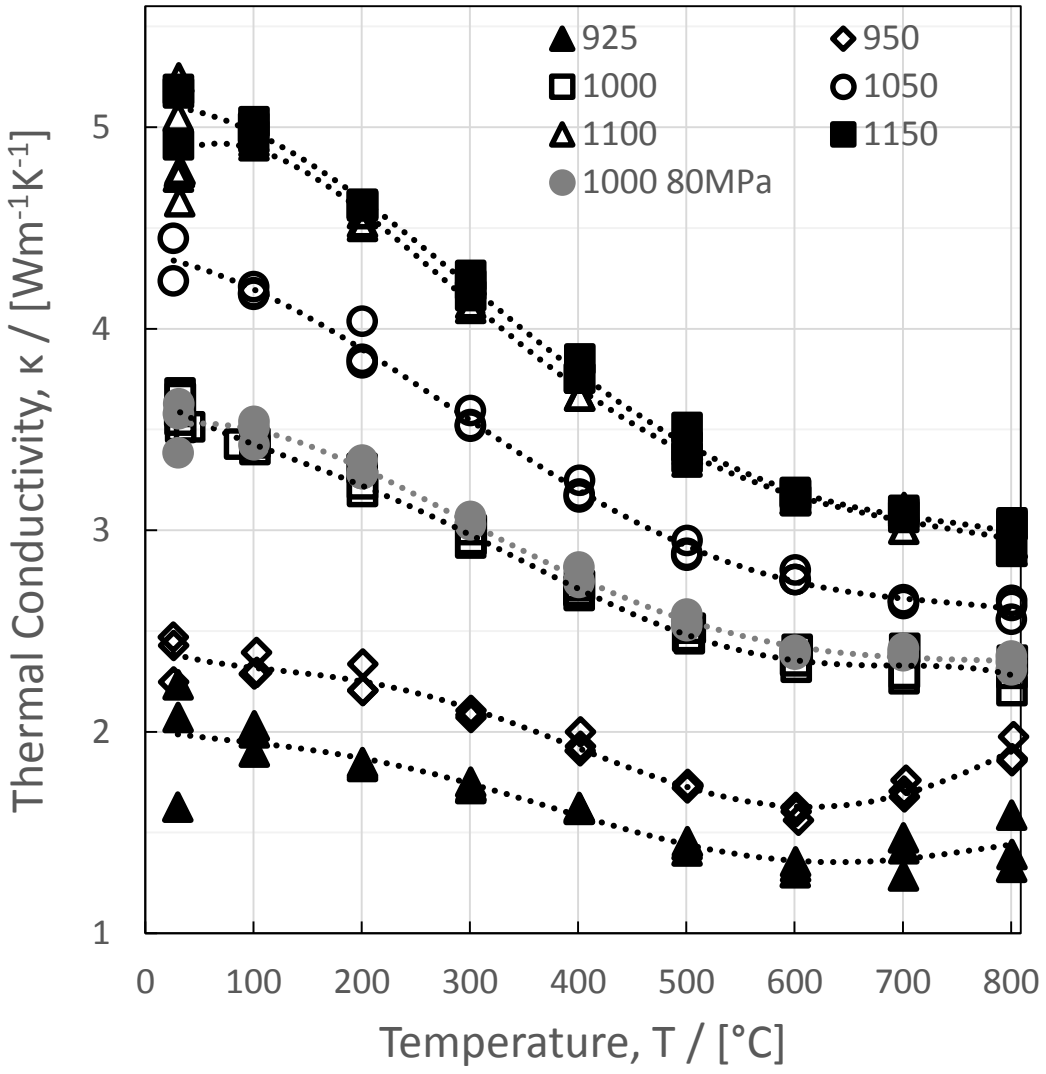

Figure 5.18: Thermal conductivity as measured by the Thermal Flash analysis method in a nitrogen atmosphere with a flow rate of approximately 50 mL/min. The dotted lines are added as a guide to the eye. All samples except the one marked with 80 MPa were sintered with a pressure of 50 MPa.

5.7 Electrical conductivity

The samples experienced some oxidation during measurement. This can be observed in Figure 5.19, as the electrical conductivity of the sample decrease significantly during the measurement, most likely because of a reduction in the charge carrier concentration. In Figure 5.20 it is displayed that the higher sintering temperatures display a higher conductivity.

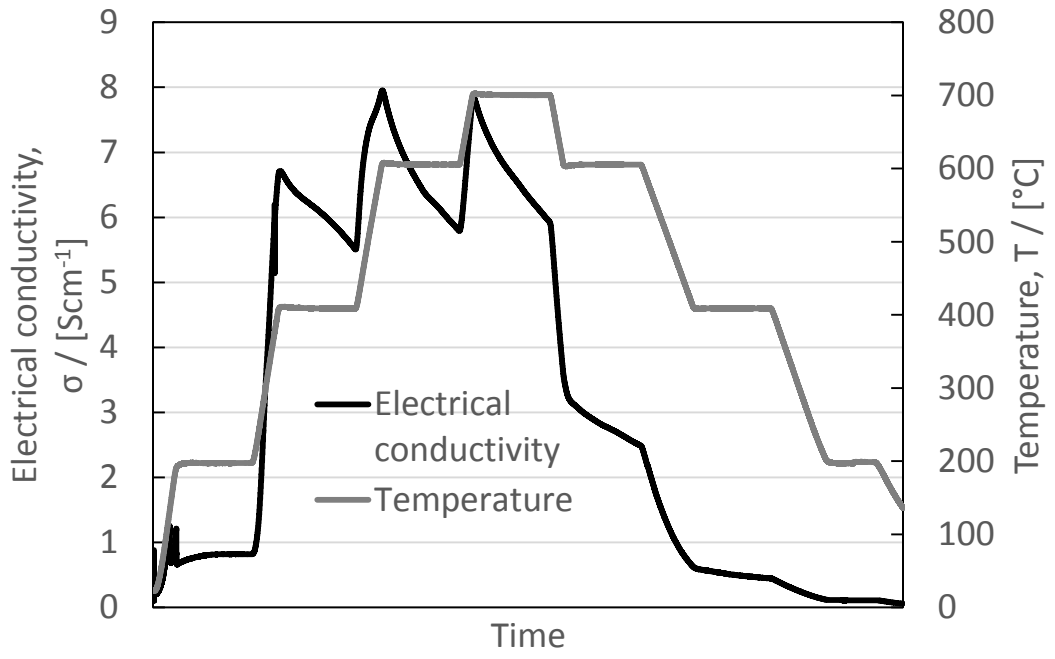

Figure 5.19: The direct results from measurements of the electrical conductivity of 1100_50_5_S3_B. As can be seen from the significant drops in conductivity at temperatures over 200°C, there is some serious problems with oxidation. The values in Figure 5.20 are taken from the peak value at each temperature step while going up in temperature.

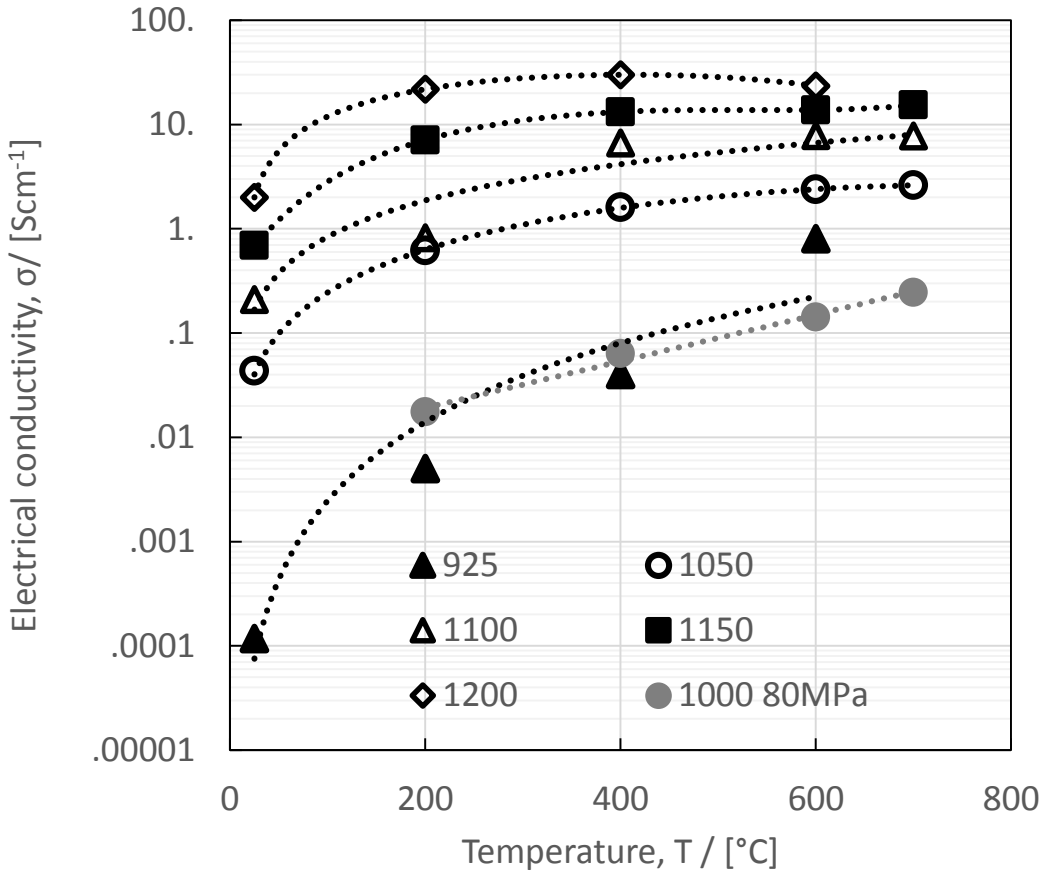

Figure 5.20: Electrical conductivity measurements of the samples as measured by the 4-point conductivity measurement method in a nitrogen atmosphere. The values are from the ascending measurements and hence the values closest to the sample after sintering. The dotted lines are added as a guide to the eye.

5.8 Seebeck measurements

As mentioned in the experimental section, there was some problem with some of these measurements. The temperature gradient used for all samples is therefore the same as for the sample sintered at 1050 °C. Even if this is an approximation, the values will not be very far from the actual values. The negative sign of the measurements come from convention, and resemble a material with n-type conduction.

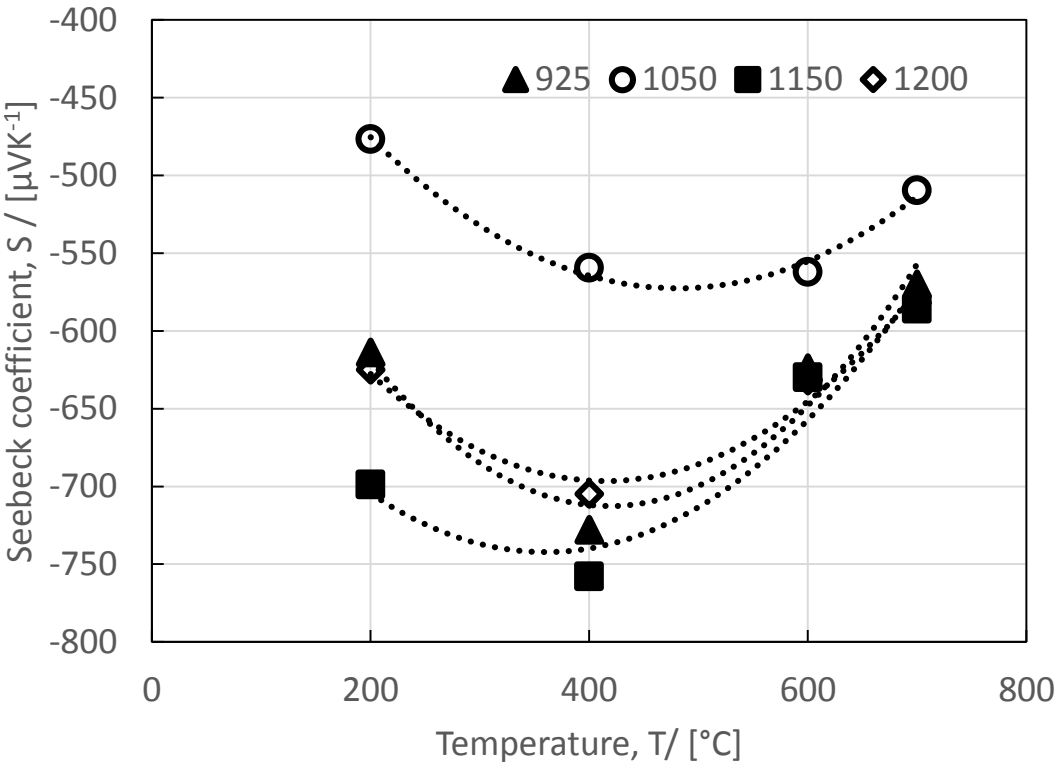

Figure 5.21: The Seebeck coefficient measured in the Probostat apparatus. Only the sample sintered at 1050 °C have the true recording of the temperature gradient. For the other samples, the same temperature gradient is used, since the difference should be minute. By convention, a negative Seebeck coefficient implies a n-type material. The dotted lines are added as a guide to the eye.

5.9 Figure of merit

Since the samples oxidized while measuring the electrical conductivity, the electrical conductivity measured on the way down in temperature are used. This is because the electrical conductivity measurements and the measurements of the Seebeck coefficients will have the closest amount of charge carriers and will therefore give the most accurate result. Contact problems during descending temperatures in the measurement of electrical conductivity gave few values that could be used in the calculation of ZT. Also, because of the error in the Seebeck coefficients, these values may be slightly different from the actual values.

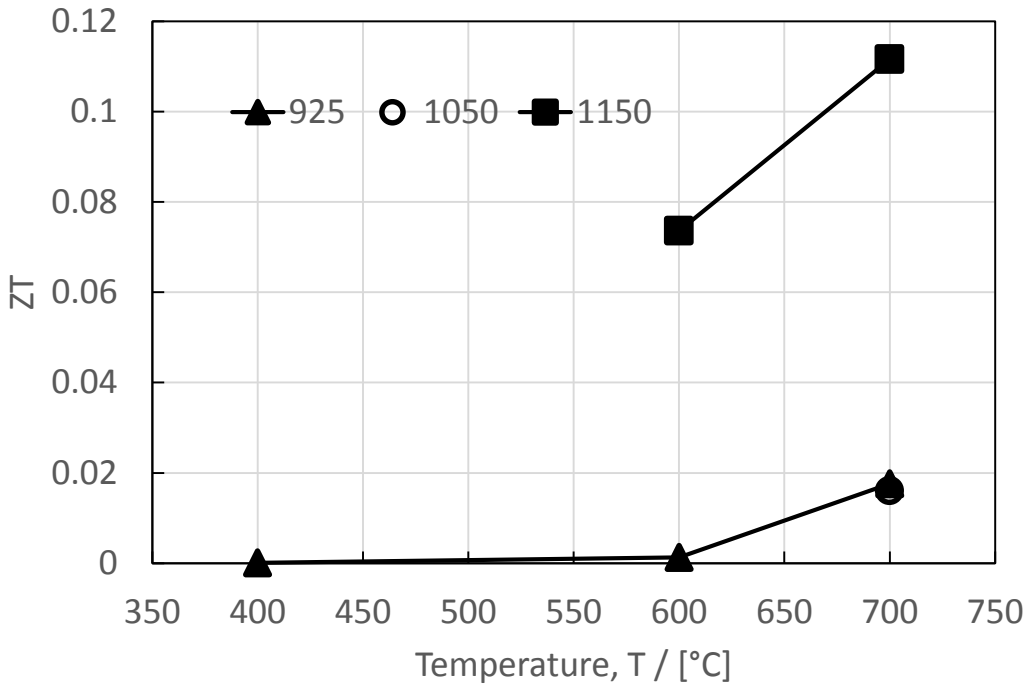

Figure 5.22: The measurements for electrical conductivity suffered some contact issues when going down in temperature for some samples. This resulted in few points in the final value of figure of merit. The lines are included as a guide to the eye.

6 Discussion

The main goal of this thesis was to reduce the thermal conductivity of the samples in order to increase the figure of merit. To be a good thermoelectric material, there are however several effects that need to be taken into account.

6.1 Densities

The spark plasma sintering have the advantage of localized heating on the interface between grains of material, where the electrical resistance is high. The applied current leads to a significant increase in local temperature and the local speed of diffusion will also increase in these areas. Even if the samples have much neck growth because of this, the grains will still have a rather big distance if no other field is applied to ensure diffusion/compaction in the bulk of the material. The reason for this is that the joule heating caused by the electrical current is strongly localized, and another field that affect the bulk material is therefore necessary. As observed in Figure 5.1, this can be either applied pressure or heat. A higher pressure, while having a sintering temperature of only 1000°C, still results in a well-compacted sample. This is most likely because of a better compaction of the powder that will lead to several more locations having neck growth because of the electrical current. Also, the material density increase with temperature because of a higher bulk diffusion rate. The TEM-photos from the sample sintered at 1200 °C show a very well sintered material with few visible pores on the micro scale.

6.2 Crystallite and grain sizes

The Figure 5.3 displays how the crystallite size of the samples change with sintering temperature. However, as these values are calculated from recorded XRD patterns, internal strain may have modified the perceived crystallite size. This becomes evident from the TEM photos of the sample sintered at 1200°C. It is easy to observe that the mean grain size of the sample is quite a bit larger than the crystallite size calculated from Scherrer's method, of about 270nm. The grain size actually seem to be closer to 1µm in this sample. Even with crystallite size being a value often associated with powders and grain size with solids[41], the difference should not be this big unless there is some additional contribution. The big difference is most likely because strain in the sample will have much the same effect as nanostructuring, in broadening the diffraction peaks of the XRD scan. The sample sintered at 950 °C do however have a grain size comparable to the values retuned by the Scherrer method, as can be seen in Figure 5.10. This might be explained by that the broadening caused by nanostructuring is dominating over the strain contribution, or that the grain shape more resemble that of a crystallite, because of less sintering. This broadening effect can also be seen with the rings forming in Figure 5.12. Even if temperature clearly gives a difference in crystallite size, it can be seen in Figure 5.3 that pressure seem to have quite little effect on this parameter. This may be because the diffusion

coefficient is affected by both temperature and time, but has no direct connection to pressure. A lower bulk diffusion coefficient will give less grain growth and Ostwald ripening. The grains will therefore remain small throughout the sintering, creating a nanostructured material, as wanted.

6.3 Oxygen diffusion

As mentioned in section 2.2, it is mainly the reduction of oxygen content in the material, which is responsible for increasing the amount of charge carriers, which happens by B-site reduction. For the material sintered at the lowest temperatures, the oxygen diffusion during sintering may become a problem, as diffusion speed is heavily dependent on temperature. A conflict of interest arise, since the diffusion of oxygen through the lattice is wanted without giving too much material diffusion in the material to cause grain growth. Unless the source material is produced in a slightly reducing atmosphere from the start, a compromise must be done between these two. There is however also indications that a higher pressure during sintering lead to a lower degree of oxygen diffusion. This is deduced from the lower electrical conductivity of the sample sintered at 1000°C and a pressure of 80 MPa, as related to the sample sintered at the same temperature with a lower pressure. Using a lower temperature and pressure, with a longer sintering time, may be an easier solution than reducing the material before sintering.

6.4 TiO_2

As explained in section 2.2.5, the level of reduction in oxygen content is the main parameter involved in determining whether exsolutions of TiO_2 will form in the sample. Since the samples sintered at the highest temperatures have the highest bulk diffusion rate it is a natural assumption that these might be the most reduced samples. This is also reflected in the XRD patterns obtained which show peaks at the reflections associated with TiO_2 for the samples sintered at the highest temperatures. The fact that TiO_2 exsolutions occur in the sample sintered at 1200 °C was visually verified in Figure 5.13. The EDS and diffraction patterns in Figure 5.14 through Figure 5.16 indicated the presence of a rutile TiO_2 phase. The reduction limit may be associated with the reduction of Ti from +4 to +3, where the local availability of new Ti-atoms to reduce is depleted, and Ti has to be removed from the primary phase in order to accommodate any further reduction, and maintain charge balance.

6.5 Thermal properties

The scattering of phonons is important in order to reduce the lattice thermal conductivity. There are several strategies to increase the amount of scattering centers in the material. For instance, doping the material heavily with a high-mass element will cause the thermal conductivity to drop. The material has a La-doping level that may contribute to this effect, but that could be further increased by more

doping. This may also aid in the electrical conductivity, as each La-dopant contribute one charge carrier by Ti-reduction. Nanostructuring the material will also supply many scattering centers in the form of grain boundaries. This effect is displayed in Figure 5.18, where a reduction in thermal conductivity with grain size is observed. By having a porous material, more scattering centers in the form of physical holes in the material, is also introduced to the material. When looking at the close match between the two samples sintered at 1000 °C, but at different pressure, it becomes evident that the grain size contribution to thermal resistivity is dominating the porosity in these samples. A lowering of thermal conductivity is observed at higher temperatures. As the temperature increase, phonon-phonon scattering start to dominate the thermal conductivity. This is observed from room temperature, to 800 °C. Some of the samples do however show an increase in thermal conductivity from 600 °C and up. Since this effect seem to occur mostly in the highly porous materials, and at high temperatures, this effect is most likely linked to radiative heat transfer inside pores. This is the only heat transfer that can occur inside pores, when assuming that there is no gas phase inside. If the charge carrier density in the material is increased, the thermal conductivity will also increase. This follows from the conductivity contribution in equation (2.27). The magnitude of this effect is also dependent on temperature, but not as much as the radiative energy transport. Its contribution may be considered low for most of the samples, as the electrical conductivity is very low. The presence of TiO_2 exsolutions showed little effect on the thermal conductivity measured, but it is difficult to say this for certain, as only one sample with TiO_2 present, was measured.

6.6 Electrical properties

The only difference in charge carrier densities between the samples is the level of oxygen reduction, since this is the only changing parameter in the stoichiometry, if not considering TiO_2-exsolution. As determined, the amount of charge carriers have a significant impact on the electrical conductivity of the samples. Even if the charge carrier density of the samples have not been measured, it can be seen qualitatively that the samples sintered at the lowest temperatures have a significantly lower electrical conductivity. From the carrier density equation presented in equation (2.19), it can be found that when the oxygen level in the material is close to 3, and even a bit oxidized, the carrier concentration go toward zero. However, just like for thermal conductivity, electric current may also be scattered. This scattering can be both lattice scattering and interactions with phonons, which is mostly dominant at higher temperatures, just like for the phonon scattering case. The impact of different parameters is however difficult to determine without having values for the charge carrier densities or electron mobility. The carrier concentration changes with the oxidation of the samples during measurement. This makes determining which other effects than the charge carrier density that have the most impact on a specific sample become even more difficult. These other effects will be small as long as the carrier density is small. The samples sintered at 1200 °C have the highest diffusion rate and

hence the highest conductivity. Lower temperatures display an electrical conductivity that is in orders of magnitude lower. The reason why the conductivities collected are lower than other values recorded in literature is most likely the high oxygen content, which give a low carrier density in the sample. The changes in grain size may also have significance, as the amount of scattering centers increase. This is, however, as mentioned, hard to determine. Having a measured level of charge carriers would display a clearer correlation between the different effects through the electron mobility. The material is experiencing big differences in conductivity because of the polaron hopping that is required, since the material do not have enough overlapping bands to have a complete conduction band. The material therefore need to have a path through the entire sample with reduced Ti-ions in order to allow the flow of an electric current. From the raw data of the measurements, it can be seen that oxidation mainly occur after moving past the level at 200 °C. This suggests that the conductivities collected at the steps below 400 °C represent the sample as received from the sintering step, without oxidation. These values are quite low, even for the most reduced samples. This suggests that the oxygen level in the samples are poorly reduced after the sintering step, and an improved sintering strategy might be favorable.

6.7 Seebeck coefficient

The Seebeck coefficient is also reliant on the charge carrier density of the samples, as seen in equation (2.11). For the Seebeck coefficient, the effect is however opposite from the electrical conductivity. A low charge carrier density is generally favored in order to get a high Seebeck coefficient. This is most likely the main reason for the high Seebeck coefficients presented in this work. Values exceeding $-500\ \mu\mathrm{VK}^{-1}$ is rare in good electrical conductors. As the most important parameters for the Seebeck coefficient of a material is its charge carrier concentration and effective electron mass, it will change by some of the same parameters as for electrical conductivity. The only way to increase electrical conductivity, without affecting the Seebeck coefficient, is by increasing the mean time between electron scattering events. Since most the samples oxidized during measurement of electrical conductivity, the Seebeck coefficient measured is a bit higher than it would be, if measured directly after sintering.

6.8 Figure of merit

The figure of merit, which determine how fit a material is for thermoelectric use, were a little lower than expected. Compared to the non-oxide materials presented in section 3.1, the figure of merit for the best sample is an order of magnitude smaller. This is mostly attributed to the low charge carrier concentration. Even with the advantage of the chemical stability that will allow a larger temperature gradient to be placed upon the thermoelectric device, the material has a low value of ZT. The

easiest path toward a higher figure of merit would be to increase the charge carrier density enough to have a decent electrical conductivity without destroying the good thermal conductivity and Seebeck coefficient. It is possible that the material will display superior properties if the charge carrier concentration is increased to a value between 10^{20} and 10^{21} cm^{-3}, as described in section 3.5.

7 Conclusion

The spark plasma sintering seem to give a good sintering density with the possibility of little grain growth. There is however some challenge with oxygen diffusion speed, when sintering for only five minutes. The content of pores in the material can have a positive effect in reducing thermal conductivity in the sample at low temperatures, but may be detrimental at higher temperatures. At lower sintering temperatures, smaller crystallites that inhibit phonon propagation and successfully decrease the phonon mean free path are found. These seem to be the main contributor to a reduced thermal conductivity. An optimum material density could be found, to reduce thermal conductivity at low temperatures, and not giving too much increase at high temperatures. The electrical conductivity of the samples were a lot smaller than intended, and oxidized during measurements. This would indicate that actual conductivities at higher temperatures might be slightly higher than the ones measured. The figure of merit is also difficult to determine for the material, as received from sintering, without measuring the Seebeck coefficient on the fresh samples, as the oxidation during measurement of electrical conductivity will change its value.

All three material parameters included in the figure of merit are to some degree dependent on the charge carrier concentration and electron mobility. With more electron-hole pair excitation at higher temperature, and increased electron mobility, the charge carrier contribution to all of these material properties are also dependent on temperature. In order to get a material with a high figure of merit, a higher charge carrier density, tuned to maximize all the parameters, should be produced. In order to be able to do this, and properly relate the material to theory, measurements of the charge carrier concentrations should be performed.

Several strategies are possible to create a material with more charge carriers. One could make a sample at low pressure, and low temperature, while increasing the holding time significantly, since diffusion is a slow process. This will increase oxygen diffusion during sintering, and lead to a higher conductivity in the finished product. Another possibility is to produce the material in a reduced state, hence introducing the carriers before sintering. This might however lead to phase segregation if reduced below the oxygen reduction limit. Whether this would be beneficial or detrimental for the material would remain to be seen. It may however also prove difficult to produce the material in a reduced state. One could also further decrease the crystallite size of the material that is sintered, to decrease diffusion lengths.

8 References

1. Sele, J., *Development of Thermoelectric n-type Oxides in the La-Sr-Ti-O-System*, in *Materials Science and Engineering*. 2013, Norwegian University of Science and Technology.
2. Rowe, D.M., *Thermoelectrics Handbook: Macro to Nano*. 2005: Taylor & Francis.
3. Pollock, D.D., *Thermoelectricity : theory, thermometry, tool / Daniel D. Pollock*. 1985, Philadelphia, PA: ASTM.
4. Mansfield, M. and C. O'Sullivan, *Understanding physics*. 1998: Wiley.
5. Kjelstrup, S. and D. Bedeaux, *Non-equilibrium Thermodynamics for Engineers*. 2010: World Scientific.
6. He, J., Y. Liu, and R. Funahashi, *Oxide thermoelectrics: The challenges, progress, and outlook.* Journal of Materials Research, 2011. **26**(15): p. 1762-1772.
7. Nag, A. and V. Shubha, *Oxide Thermoelectric Materials: A Structure–Property Relationship.* Journal of Electronic Materials, 2014. **43**(4): p. 962-977.
8. Fergus, J.W., *Oxide materials for high temperature thermoelectric energy conversion.* Journal of the European Ceramic Society, 2012. **32**(3): p. 525-540.
9. ZHANG, L., et al., *Thermoelectric properties of combustion synthesized and spark plasma sintered Sr[1-] [x]R[x]TiO[3] (R = Y, La, Sm, Gd, Dy, 0 < x ≤ 0.1)*. Vol. 48. 2007, Sendai, JAPON: Japan Institute of Metals. 6.
10. Cutler, M., J.F. Leavy, and R.L. Fitzpatrick, *Electronic Transport in Semimetallic Cerium Sulfide.* Physical Review, 1964. **133**(4A): p. A1143-A1152.
11. Moore, J.P. and R.S. Graves, *Absolute Seebeck coefficient of platinum from 80 to 340 K and the thermal and electrical conductivities of lead from 80 to 400 K.* Journal of Applied Physics, 1973. **44**(3): p. 1174-1178.
12. K.Momma and F. Izumi, *VESTA 3 for three-dimensional visualization of crystal, volumetric and morphology data.* Journal of Applied Crystallography, 2011(44): p. 1272-1276.
13. Shannon, R., *Revised effective ionic radii and systematic studies of interatomic distances in halides and chalcogenides.* Acta Crystallographica Section A, 1976. **32**(5): p. 751-767.
14. Ubic, R., et al., *The Effect of A-Site Vacancies on Cell Volume and Tolerance Factor of Perovskites*, in *Processing and Properties of Advanced Ceramics and Composites V*. 2013, John Wiley & Sons, Inc. p. 331-336.
15. Liu, X., R. Hong, and C. Tian, *Tolerance factor and the stability discussion of ABO3-type ilmenite.* Journal of Materials Science: Materials in Electronics, 2009. **20**(4): p. 323-327.
16. Burnat, D., et al., *Synthesis and performance of A-site deficient lanthanum-doped strontium titanate by nanoparticle based spray pyrolysis.* Journal of Power Sources, 2012. **201**(0): p. 26-36.
17. Neagu, D. and J.T.S. Irvine, *Enhancing Electronic Conductivity in Strontium Titanates through Correlated A and B-Site Doping.* Chemistry of Materials, 2011. **23**(6): p. 1607-1617.
18. Neagu, D. and J.T.S. Irvine, *Structure and Properties of La0.4Sr0.4TiO3 Ceramics for Use as Anode Materials in Solid Oxide Fuel Cells.* Chemistry of Materials, 2010. **22**(17): p. 5042-5053.
19. Blennow, P., et al., *Effects of Sr/Ti-ratio in SrTiO3-based SOFC anodes investigated by the use of cone-shaped electrodes.* Electrochimica Acta, 2006. **52**(4): p. 1651-1661.
20. Cho, S.G. and P.F. Johnson, *Evolution of the microstructure of undoped and Nb-doped SrTiO3.* Journal of Materials Science, 1994. **29**(18): p. 4866-4874.

21. Moos, R. and K.H. Hardtl, *Defect Chemistry of Donor-Doped and Undoped Strontium Titanate Ceramics between 1000° and 1400°C.* Journal of the American Ceramic Society, 1997. **80**(10): p. 2549-2562.
22. Marina, O.A., N.L. Canfield, and J.W. Stevenson, *Thermal, electrical, and electrocatalytical properties of lanthanum-doped strontium titanate.* Solid State Ionics, 2002. **149**(1–2): p. 21-28.
23. Streetman, B.G. and S.K. Banerjee, *Solid State Electronic Devices*. 2006: Pearson Prentice Hall.
24. Moos, R., A. Gnudi, and K.H. Härdtl, *Thermopower of Sr1−xLaxTiO3 ceramics.* Journal of Applied Physics, 1995. **78**(8): p. 5042-5047.
25. Kittel, C. and P. McEuen, *Introduction to Solid State Physics*. 8th ed. 2005: Wiley. 680.
26. Altin, S., et al., *Thermal conductivity and magnetic properties of the B substituted Ca3Co4O9.* Current Applied Physics, 2014. **14**(4): p. 590-595.
27. Ashida, T., et al., *Thermal transport properties of polycrystalline tin-doped indium oxide films.* Journal of Applied Physics, 2009. **105**(7): p. -.
28. Kumar, G.S., G. Prasad, and R.O. Pohl, *Experimental determinations of the Lorenz number.* Journal of Materials Science, 1993. **28**(16): p. 4261-4272.
29. Bréchignac, C. and P. Houdy, *Nanomaterials and Nanochemistry*. 2008: Springer.
30. Wan, C., et al., *Thermal conductivity of superplastically deformed 3Y-TZP.* Materials Transactions, 2002. **43**(10): p. 2473-2479.
31. Tokita, M., *Chapter 11.2.3 - Spark Plasma Sintering (SPS) Method, Systems, and Applications*, in *Handbook of Advanced Ceramics (Second Edition)*, S. Somiya, Editor. 2013, Academic Press: Oxford. p. 1149-1177.
32. Snyder, G.J. and E.S. Toberer, *Complex thermoelectric materials.* Nat. Mater., 2008. **7**(2): p. 105-114.
33. Dang, F., et al., *Thermoelectric Performance of SrTiO3 Enhanced by Nanostructuring—Self-Assembled Particulate Film of Nanocubes.* ACS Applied Materials & Interfaces, 2013. **5**(21): p. 10933-10937.
34. Lee, J. and Y. Shul, *Physical and electrochemical properties of (La0.3Sr0.7)0.93TiO3–δ synthesized by Pechini method as an anode material for solid oxide fuel cells.* Journal of Sol-Gel Science and Technology, 2014. **69**(1): p. 148-154.
35. Loland, T.E., *Development of oxide based thermoelectric materials*, in *Materials Science and Engineering*. 2013, Norwegian Universiy of Technology and Science.
36. Koumoto, K., et al., *Oxide 'Thermoelectric Materials: A Nanostructuring Approach*, in *Annual Review of Materials Research, Vol 40*, D.R. Clarke, M. Ruhle, and F. Zok, Editors. 2010. p. 363-394.
37. Savaniu, C.-D. and J.T.S. Irvine, *Reduction studies and evaluation of surface modified A-site deficient La-doped SrTiO3 as anode material for IT-SOFCs.* Journal of Materials Chemistry, 2009. **19**(43): p. 8119-8128.
38. Dughaish, Z.H., *Lead telluride as a thermoelectric material for thermoelectric power generation.* Physica B: Condensed Matter, 2002. **322**(1–2): p. 205-223.
39. Eberg, E., et al., *Comparison of TEM specimen preparation of perovskite thin films by tripod polishing and conventional ion milling.* Journal of electron microscopy, 2008. **57**(6): p. 175-179.
40. Patterson, A.L., *The Scherrer Formula for X-Ray Particle Size Determination.* Physical Review, 1939. **56**(10): p. 978-982.
41. Suresh, A., et al., *Crystallite and Grain-Size-Dependent Phase Transformations in Yttria-Doped Zirconia.* Journal of the American Ceramic Society, 2003. **86**(2): p. 360-362.

9 APPENDIX

9.1 Sample names

Table 9.1: A total overview of the sample names and their process parameters during sintering.

Sample name	Sintering temperature [°C]	Pressure [MPa]	Sample number	Powder batch
900_50_5_S1_A	900	50	1	C2_HI_B
925_50_5_S1_C	925	50	1	CM_LO_B
925_50_5_S2_C	925	50	2	CM_LO_B
950_50_5_S1_A	950	50	1	C2_HI_B
950_50_5_S2_A	950	50	2	C2_HI_B
950_50_5_S3_B	950	50	3	CM_HI_B
1000_50_5_S1_A	1000	50	1	C2_HI_B
1000_50_5_S2_A	1000	50	2	C2_HI_B
1000_50_5_S3_B	1000	50	3	CM_HI_B
1050_50_5_S1_A	1050	50	1	C2_HI_B
1050_50_5_S2_A	1050	50	2	C2_HI_B
1050_50_5_S3_B	1050	50	3	CM_HI_B
1100_50_5_S1_A	1100	50	1	C2_HI_B
1100_50_5_S2_A	1100	50	2	C2_HI_B
1100_50_5_S3_B	1100	50	3	CM_HI_B
1100_50_5_S4_B	1100	50	4	CM_HI_B
1100_50_5_S5_B	1100	50	5	CM_HI_B
1150_50_5_S1_A	1150	50	1	C2_HI_B
1150_50_5_S2_A	1150	50	2	C2_HI_B
1150_50_5_S3_B	1150	50	3	CM_HI_B
1150_50_5_S4_B	1150	50	4	CM_HI_B
1150_50_5_S5_C	1150	50	5	CM_LO_B
1200_50_5_S1_A	1200	50	1	C2_HI_B
1200_50_5_S2_A	1200	50	2	C2_HI_B
1200_50_5_S3_B	1200	50	3	CM_HI_B
1200_50_5_S4_B	1200	50	4	CM_HI_B
950_80_5_S1_B	950	80	1	CM_HI_B
1000_70_5_S1_B	1000	70	1	CM_HI_B
1000_80_5_S1_B	1000	80	1	CM_HI_B

9.2 Densities

Table 9.2: The densities of the measured samples. Some of the samples deviate from the other with the same process values, this is probably because of the increased error in using a lighter sample and thereby increasing potential errors. There might be an error of +/- 1% in the measurements because of human handling. For the theoretical density the same value is used for all the samples, namely 5.1595 g/cm^3. Because of instrumental difficulties, a few samples did not get measured.

Sample	Density, g/cm^3	% of theoretical	Open porosity	Closed porosity
900_50_5_S1_A	3,784	73,33	22,13	4,54
925_50_5_S1_C	4,191	81,23	15,08	3,69
950_50_5_S1_A	4,280	82,96	11,94	5,11
950_50_5_S2_A	4,219	81,78	16,34	1,88
1000_50_5_S1_A	4,749	92,04	1,15	6,80
1000_50_5_S2_A	4,783	92,70	0,56	6,74
1050_50_5_S1_A	5,037	97,62	0,39	1,98
1050_50_5_S2_A	4,928	95,50	0,59	3,90
1100_50_5_S1_A	5,062	98,10	0,90	1,00
1100_50_5_S2_A	5,077	98,41	0,48	1,11
1100_50_5_S3_B	5,056	98,00	0,88	1,12
1150_50_5_S1_A	5,102	98,88	0,39	0,72
1150_50_5_S2_A	4,943	95,80	0,74	3,46
1150_50_5_S3_B	4,929	95,52	1,60	2,88
1150_50_5_S4_B	5,021	97,32	0,84	1,84
1200_50_5_S1_A	5,074	98,35	1,02	0,63
1200_50_5_S2_A	5,037	97,63	0,23	2,14
1200_50_5_S3_B	4,999	96,88	1,03	2,09
1200_50_5_S4_B	5,023	97,36	0,33	2,31
950_80_5_S1_B	4,825	93,52	0,75	5,73
1000_70_5_S1_B	4,957	96,08	0,39	3,53
1000_80_5_S1_B	5,022	97,33	0,55	2,12

9.3 Seebeck coefficients for Pt

Table 9.3: The Seebeck coefficients at different temperatures for Pt[11].

Temperature [K]	Seebeck coefficient for Platinum [µV/K]
280	-4,53
300	-5,15
320	-5,72
400	-6,25
500	-9,68
600	-11,33
700	-12,87
800	-14,38
900	-15,97
1000	-17,58
1100	-19,03
1200	-20,56